Article

Cell Systems

TAMEP are brain tumor parenchymal cells controlling neoplastic angiogenesis and progression

Graphical Abstract

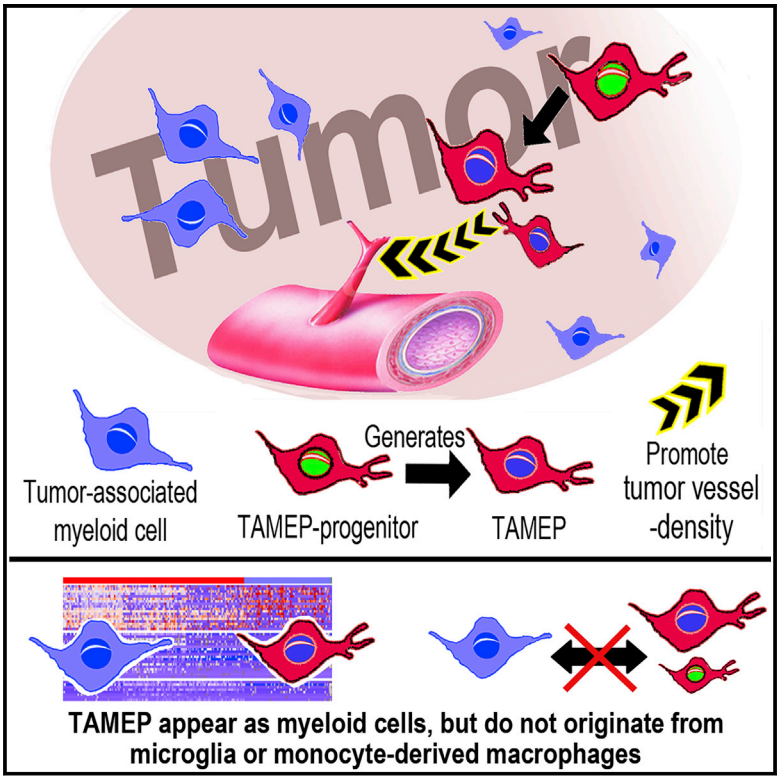

Highlights

- Uncovering brain tumor-associated cells with a myeloid expression profile (TAMEP)
- TAMEP appear as a myeloid population but do not derive from microglia or bone marrow
- TAMEP originate from local progenitors activated by brain tumors
- TAMEP promote tumor expansion by enhancing vessel density

Authors

Roland E. Kälin, Linzhi Cai, Yuping Li, ..., Christian Schulz, Ines Hellmann, Rainer Glass

Correspondence

rainer.glass@med.uni-muenchen.de

In Brief

The rapid expansion of aggressive brain tumors is supported by the tumor parenchyma including blood vessels and myeloid cells (CNS- or bone-marrow-derived macrophages). Our study reveals TAMEP as a cell subset in the brain tumor microenvironment, which is generated by progenitor cells in the CNS. TAMEP have a myeloid appearance but do not originate from CNS or peripheral macrophages. TAMEP strongly support pathological angiogenesis and promote brain tumor growth.

Kälin et al., 2021, Cell Systems *12*, 248–262
March 17, 2021
https://doi.org/10.1016/j.cels.2021.01.002

CellPress

CellPress
OPEN ACCESS

Cell Systems

Article

TAMEP are brain tumor parenchymal cells controlling neoplastic angiogenesis and progression

Roland E. Kälin,[1,2,13] Linzhi Cai,[1,2,13,14] Yuping Li,[1,2] Dongxu Zhao,[1,2] Huabin Zhang,[1,2] Jiying Cheng,[1,2] Wenlong Zhang,[2,3] Yingxi Wu,[1,2] Katharina Eisenhut,[1,2] Philipp Janssen,[4] Lukas Schmitt,[4] Wolfgang Enard,[4] Friederike Michels,[5] Charlotte Flüh,[5] Mengzhuo Hou,[1,2] Sabrina V. Kirchleitner,[6] Sebastian Siller,[6] Matthias Schiemann,[7] Immanuel Andrä,[7] Eloi Montanez,[2,8] Claudio Giachino,[9] Verdon Taylor,[9] Michael Synowitz,[5] Jörg-Christian Tonn,[6,10] Louisa von Baumgarten,[2,3,6] Christian Schulz,[2,11,12] Ines Hellmann,[4] and Rainer Glass[1,2,10,15,*]

[1]Neurosurgical Research, University Hospital, LMU Munich, 81377 Munich, Germany
[2]Walter-Brendel-Centre of Experimental Medicine, University Hospital, LMU Munich, 81377 Munich, Germany
[3]Department of Neurology, University Hospital, LMU Munich, 81377 Munich, Germany
[4]Anthropology and Human Genomics, Department Biology II, LMU Munich, 82152 Planegg-Martinsried, Germany
[5]Department of Neurosurgery, University Hospital Center Schleswig Holstein, 24105 Kiel, Germany
[6]Department of Neurosurgery, University Hospital, LMU Munich, 81377 Munich, Germany
[7]Institute for Medical Microbiology, Immunology and Hygiene, Technische Universität München, 81675 München, Germany
[8]Department of Physiological Sciences, Faculty of Medicine and Health Sciences, University of Barcelona and Bellvitge Biomedical Research Institute (IDIBELL), 08907 Hospitalet de Llobregat, Spain
[9]Department of Biomedicine, University of Basel, 4058 Basel, Switzerland
[10]German Cancer Research Center (DKFZ), German Cancer Consortium (DKTK), Partner Site Munich, 69120 Heidelberg, Germany
[11]Medizinische Klinik und Poliklinik I, University Hospital, LMU Munich, 81377 Munich, Germany
[12]German Centre for Cardiovascular Research (DZHK), Partner Site Munich Heart Alliance, 80333 Munich, Germany
[13]These authors contributed equally
[14]Present address: Department of Neurosurgery, Renmin Hospital of Wuhan University, Wuhan 430060, China
[15]Lead contact
*Correspondence: rainer.glass@med.uni-muenchen.de
https://doi.org/10.1016/j.cels.2021.01.002

SUMMARY

Aggressive brain tumors like glioblastoma depend on support by their local environment and subsets of tumor parenchymal cells may promote specific phases of disease progression. We investigated the glioblastoma microenvironment with transgenic lineage-tracing models, intravital imaging, single-cell transcriptomics, immunofluorescence analysis as well as histopathology and characterized a previously unacknowledged population of tumor-associated cells with a myeloid-like expression profile (TAMEP) that transiently appeared during glioblastoma growth. TAMEP of mice and humans were identified with specific markers. Notably, TAMEP did not derive from microglia or peripheral monocytes but were generated by a fraction of CNS-resident, SOX2-positive progenitors. Abrogation of this progenitor cell population, by conditional *Sox*2-knockout, drastically reduced glioblastoma vascularization and size. Hence, TAMEP emerge as a tumor parenchymal component with a strong impact on glioblastoma progression.

INTRODUCTION

The microenvironment of primary, malignant brain tumors (glioblastoma; GBM) can strongly support neoplastic progression (Aldape et al., 2019). The GBM parenchyma consists of a complex mix of brain resident as well as immigrating cells (Aldape et al., 2019; Glass and Synowitz, 2014; Hambardzumyan et al., 2016) including subsets of stem and progenitor cells (Audia et al., 2017; Stock et al., 2012). A range of pathologically relevant effects mediated by mesenchymal stem cells (MSCs), neural precursor cells (NPCs), or oligodendrocyte progenitor cells (OPCs) have been reported (Audia et al., 2017; Huang et al., 2014; Stock et al., 2012). MSCs have tumor-supporting or anti-neoplastic functions potentially owing to their origins in the bone marrow or in local perivascular positions (Audia et al., 2017; Behnan et al., 2014; Ho et al., 2013). NPCs curtail GBM progression by the release of bioactive lipids (Stock et al., 2012), but the number of NPCs declines with age, and therefore, NPC-induced GBM suppression is restricted to the young brain and lost at postnatal day 90 (P90) in mice (Walzlein et al., 2008). OPCs can contribute to perivascular cells in GBM and thereby support neovascularization (Huang et al., 2014). However, it is

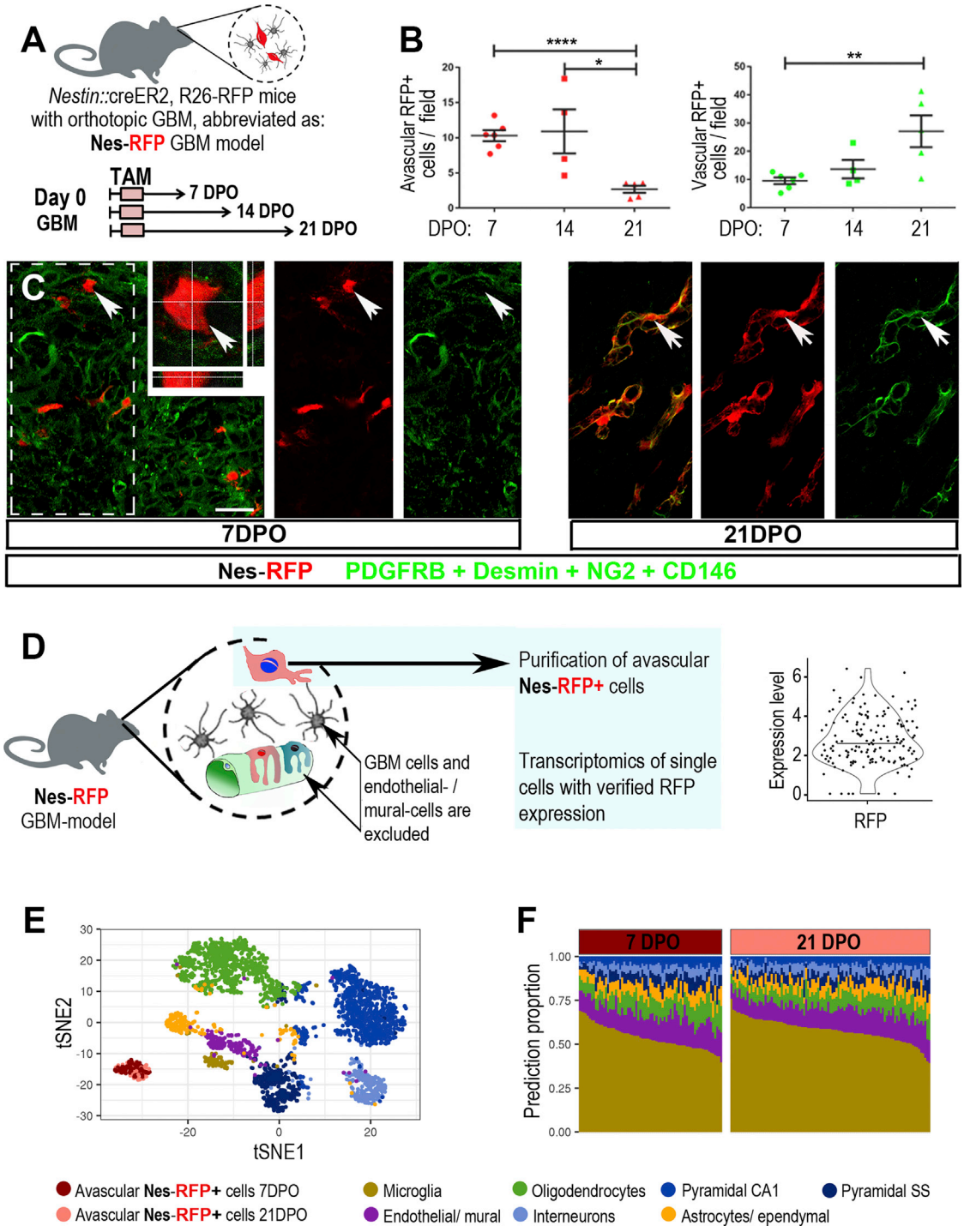

Figure 1. A model for tracing tumor-associated cells with a myeloid-like expression profile (TAMEP)

(A) Nes-RFP mice bearing orthotopic glioma were inspected at 7, 14, or 21 DPO.

(B) Quantity of RFP+ cells in an avascular (left) and a vessel-associated (right) position (each dot indicates data from one mouse: n = 6 at 7DPO, n = 4 at 14DPO, and n = 5 at 21 DPO).

(C) Immunofluorescence for pericyte markers (in unison shown in green); at 7DPO pericyte marker-negative RFP+ cells predominate, arrow corresponds to single-channel micrographs (dashed line) and orthogonal view; at 21 DPO RFP+, cells are pericyte marker positive.

(D) Purified cells from orthotopic glioma showed strong RFP expression; in $\log_2$(CPM).

(E) A t-SNE plot of classified mouse brain cells combined with our scRNA-seq data.

(legend continued on next page)

currently unclear if other (e.g., tissue resident) pools of stem and progenitor cells contribute to GBM progression.

Vascular cells as well as tumor-associated myeloid cells constitute the major components of the GBM parenchyma (Aldape et al., 2019; Audia et al., 2017). Myeloid cells, which consist of microglia and peripheral macrophages, accelerate GBM cell-invasion (Glass and Synowitz, 2014; Hambardzumyan et al., 2016) and the rich vascular network of GBM has important tumor-trophic functions (Aldape et al., 2019; Audia et al., 2017). Microglia are ontogenetically distinct from bone-marrow-derived immune cells, but otherwise share the cellular plasticity, innate immune functions, and sets of markers with peripheral macrophages (Hammond et al., 2018; Prinz et al., 2017). Under physiological conditions, the bone marrow contributes only to ventricular (choroid plexus) macrophages but not to other pools of CNS phagocytes (Goldmann et al., 2016), while large numbers of peripheral immune cells can accumulate in the brain during neuropathology (Glass and Synowitz, 2014; Hambardzumyan et al., 2016; Hammond et al., 2018; Prinz et al., 2017).

While the role of tumor-associated myeloid cells on GBM progression is well documented, we have only partial knowledge of the pathological impact of GBM-parenchymal progenitor cells. Therefore, we investigated the GBM microenvironment using a transgenic lineage-tracing model indicating progenitor cells of the brain and their progeny (Giachino and Taylor, 2009). Detailed inspection of this cell subset revealed a previously unacknowledged population of GBM-associated cells with a myeloid expression profile. This newly identified set of myeloid-like cells derives from local progenitors without any contribution from the bone marrow. Hence, this cell subset is clearly distinct from microglia or monocyte-derived macrophages. We show that this population supports tumor growth in murine models of GBM by inducing angiogenesis.

RESULTS

Tracing a subpopulation of myeloid-like cells in GBM

GBM-associated progenitor cells may modulate the course of disease progression, but data on the intratumoral fate of progenitor-derived cell types are sparse. Mouse strains for tamoxifen-induced cre-recombinase expression under the control of various nestin gene-promoters (*Nestin*::creER2) allow tracing of CNS-resident progenitors (and their progeny), for e.g., NPC, OPC, and partly also of pericytes (Sun et al., 2014), which share characteristics with MSC (Crisan et al., 2008; Sun et al., 2014). All these cell types are part of the GBM microenvironment (Audia et al., 2017; Huang et al., 2014; Stock et al., 2012). Animal models containing genetically modified gene-promoter elements for the intermediate filament Nestin allow transgene expression preponderantly in stem and progenitor cells (Giachino and Taylor, 2009). Nestin promoter controlled expression of cre recombinase fused with a mutant estrogen receptor (creER2) permits tamoxifen-induced (timed) transgene expression (Giachino and Taylor, 2009). In combination with cre-mediated excision of a loxP-flanked (floxed) stop codon driving the expression of a fluorescent reporter (tdTomato; RFP), this provides a system for inheritable cell labeling (Madisen et al., 2010). Initially, we compared two *Nestin*::creER2 mouse strains (Giachino and Taylor, 2009; Lagace et al., 2007) and chose the model (abbreviated as Nes-RFP mice) with superior sensitivity and specificity as an experimental model (Figures S1A–S1C). Nes-RFP mice traced larger numbers of intratumoral cells (Figure S1D) that were negative for the astrocyte-marker glial fibrillary acidic protein (GFAP) (Figure S1E) and were non-leaky (Figure S1F; see Tables S1 and S2 for details on all models). NPC-migration to GBM is restricted to the young brain (before postnatal day 90; P90) and we excluded effects of tumor-associated NPCs by using mice of P100 or older for all experiments (Stock et al., 2012; Walzlein et al., 2008). Thereby, we obtained a technically sound model for tracing of tumor parenchymal cells from a Nestin-positive source without contribution by astrocytes or NPCs.

Experiments were performed according to the experimental schedule in Figure 1A and inspection over a time course showed a number of traced (RFP+) avascular cells, whose numbers declined during tumor progression (from 7 to 21 days post-operatively; DPO), whereas a population of vascular RFP+ cells increased (Figure 1B). Immunofluorescence for platelet-derived growth factor-B (PDGFRB), Desmin, neural/glial antigen-2 (NG2), and CD146 (Armulik et al., 2011) identified vessel-associated RFP+ cells as pericytes (Figures 1C and S1G–S1N), whereas avascular cells were not labeled for pericyte markers (Figure 1C). Intravital imaging of traced cells during glioma expansion over a time course of 3 weeks and longer showed that both sets of cells remained in their respective localization (Figure S2), thereby excluding the possibility that avascular RFP+ cells may acquire a pericyte identity throughout tumor growth or that pericytes detach from vessels. Of note, this also shows that traced cells in our study are different from OPCs, which exert a pathological role in GBM by contributing perivascular cells form an avascular source (Huang et al., 2014).

In order to uncover the identity of the non-vascular RFP+ cells, we purified these by flow cytometry from experimental gliomas at 7 and 21 DPO and analyzed them by single-cell transcriptomics (scRNA-seq; Figures 1D–1F). Note that due to the tight association with blood vessels, vascular RFP+ cells were excluded by our cell-isolation protocol (Bondjers et al., 2006). Cells were processed using SCRB-seq, a sensitive 3′-tagged RNA-seq protocol (Parekh et al., 2018; Ziegenhain et al., 2017), and we obtained high-quality single-cell expression profiles with 6,000 to 50,000 transcripts for 155 out of 180 processed cells with confirmed RFP expression (Figure 1D). Integrating our RFP+ avascular cells with the expression profiles of over 3,000 neuronal and non-neuronal cells from the mouse brain (Zeisel et al., 2015) within a t-distributed stochastic neighbor embedding (t-SNE) plot showed that they form a homogeneous cell fraction (Figure 1E) and a classification algorithm suggested a similarity with microglia (Figure 1F). In summary, this indicates that our Nes-RFP

(F) A random-forest analysis indicated a high statistical proximity of traced avascular cells with microglia at 7 and 21 DPO. All immunofluorescence data were retrieved with $n \geq 4$ mice per group and scRNA-seq analysis was performed with n = 6 animals. Scale bar is 50 μm; data (in B) are presented as mean ± SD; statistical significance was determined by one-way ANOVA with post hoc test and is indicated as follows: *$p < 0.05$, **$p < 0.01$, ****$p < 0.0001$. See also Figures S1 and S2.

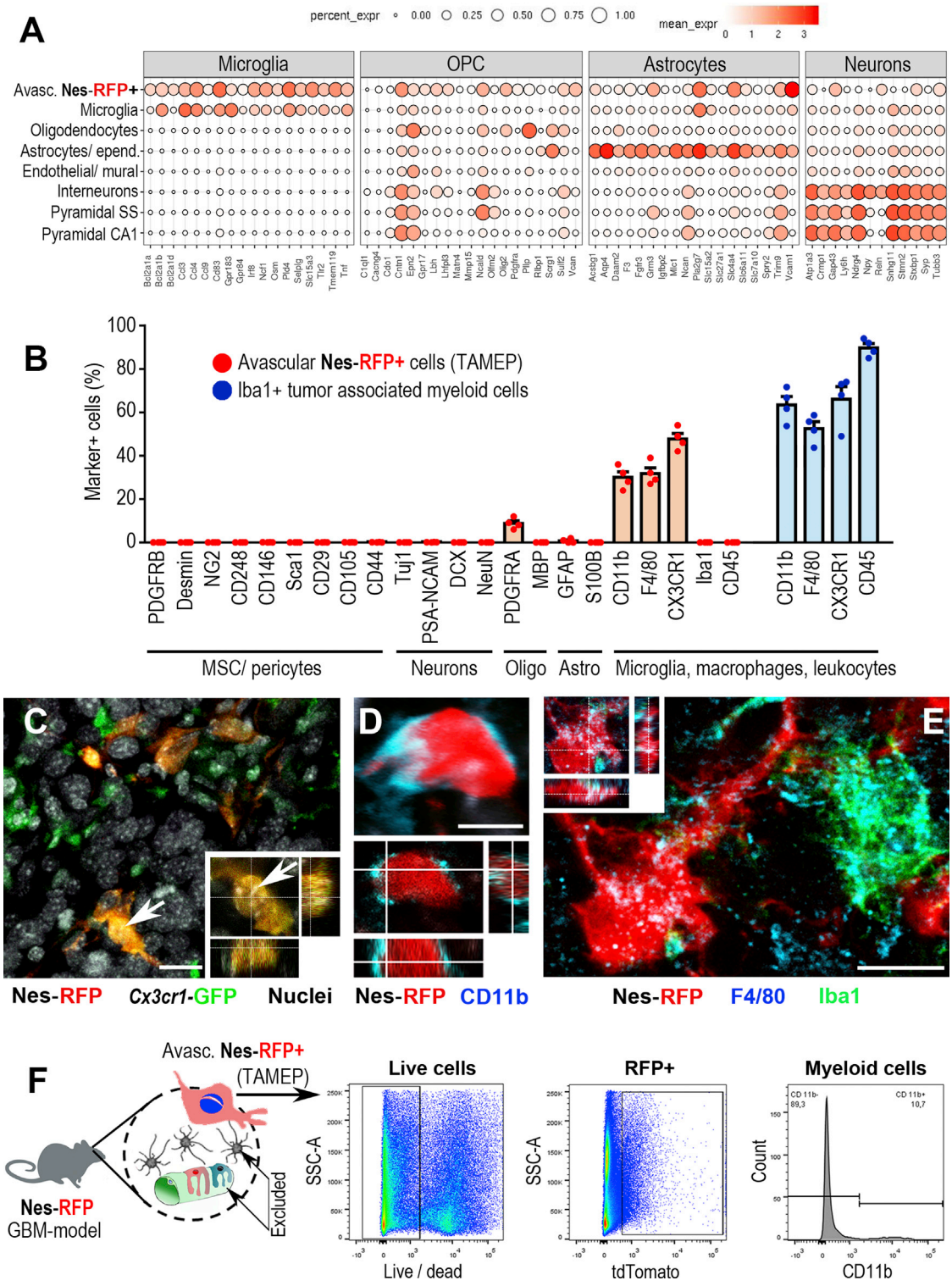

Figure 2. Traced myeloid-like cells express phagocyte markers but differ from microglia or macrophages

(A) ScRNA-seq data indicate that avascular RFP+ cells (Avasc. RFP+; TAMEP) express microglia or some OPC markers.

(B) Immunofluorescence markers in avascular RFP+ cells (at 14 DPO; as compared with Iba1+ myeloid cells; each dot indicates data from one mouse; n = 4 animals in all groups).

(C) Nes-RFP, *Cx3cr1*-GFP glioma models corroborate myeloid differentiation of RFP+ avascular cells at 7 DPO (a single cell is shown in orthogonal view; arrow).

(D) Three-dimensional and orthogonal view of a traced avascular cell (within a glioma; Nes-RFP strain) expressing CD11b at 7 DPO.

(legend continued on next page)

strain traced a transient population of intratumoral cells, which stably remained in a non-vascular position and acquired a microglia-like transcription profile.

Characterization of TAMEP

Single-cell gene expression levels for traced avascular cells (Figure 2A) were compared with established gene expression profiles for microglia, OPCs, astrocytes, or neurons and confirmed that traced avascular cells have high similarity with microglia (plus a minor overlap with OPC; Figure 2A). In addition, we quantified immuno-positivity for a range of cell-lineage-identifying molecules (Armulik et al., 2010; Hammond et al., 2018; Jones and Schäfer, 2015; Kovacs, 2017; Prinz et al., 2017) in traced avascular cells (Figure 2B) and found that these were different from pericytes, MSC, mature/immature neurons or astrocytes (Astro). PDGFRA (an OPC marker) was expressed in a subset of RFP+ avascular cells, whereas myelin basic protein (MBP; for mature oligodendrocytes; Oligo) was absent; several key-markers for microglia (CD11b, F4/80, and CX3CR1) were abundant, but other canonical markers for myeloid cells like Iba1 and CD45 were not found (whereas Iba1+ tumor-associated myeloid cells abundantly expressed CD11b, F4/80, CX3CR1, and CD45; Figure 2B). Additional evidence, that traced avascular cells have a myeloid appearance (Figure 2C), was obtained after crossbreeding Nes-RFP mice with the *Cx3cr1*-GFP strain, which reliably identifies macrophages (Jung et al., 2000; Mizutani et al., 2012). Coherently, we detected immuno-positivity (Figures 2D and 2E) for myeloid (CD11b) and macrophage (F4/80) markers (Van Hove et al., 2019) in traced RFP+ cells. Flow cytometry analysis of traced avascular cells from orthotopic gliomas at 14 DPO fully substantiated that viable, traced avascular cells can express myeloid markers on the protein level (Figures 2F and S3). Altogether, scRNA-seq of traced, avascular RFP+ cells revealed a GBM-parenchymal, atypical myeloid component (hereafter referred to as tumor-associated cells with a myeloid-like expression profile; TAMEP). Immunofluorescence, reporter mouse strains, and FACS confirmed that TAMEP resemble myeloid cells.

TAMEP derive from Sox2-dependent progenitors

So far our study characterized TAMEP as a transient, myeloid-like subset of cells, which are largely confined to earlier/intermediate phases of glioma growth. Modification of the tamoxifen-schedule revealed that TAMEP could be traced from different time points (1 DPO or 7 DPO) of gliomagenesis, while injection of tamoxifen into tumor-free animals followed by a chase period and implantation of tumors thereafter did not yield traced cells (Figure 3A). This suggests that our model specifically traced TAMEP in a disease context and that this cell population is not present in the healthy brain. Labeling with thymidine analogs showed that TAMEP are proliferative and can repetitively enter the cell cycle (Figure 3B). We reasoned that this may imply that TAMEP originates from a progenitor through activation by a pathological stimulus, followed by rapid expansion. Therefore, we investigated the expression of stem and progenitor cell markers in traced intratumoral cells of Nes-RFP mice (Figures 3C and 3D). Indeed, we detected an expression of the stem cell transcription factor SOX2 (Sarkar and Hochedlinger, 2013) in avascular RFP+ cells (Figure 3C) but never in vascular RFP+ cells (Figure 3D). Next, we asked if SOX2 has a particular biological role in avascular RFP+ cells and induced a conditional *Sox2*-knockout (Shaham et al., 2009) using our Nes-RFP mouse strain (*Nestin*::creER2, R26-RFP, *Sox2*$^{fl/fl}$; as compared with Nes-RFP controls) after tumor inoculation (Figure 3E). Remarkably, we observed that *Sox2*-loss diminished the number of RFP+ avascular cells in gliomas. In particular, we found that traced avascular cell numbers were very strongly reduced in *Nestin*::creER2, R26-RFP, Sox2$^{fl/fl}$ mice at 14 DPO (in average 2.07 cells per counting frame in knockouts as compared with 10.9 cells per frame in wild-type controls). At 7 DPO, a tendency for a reduction in avascular RFP+ cell numbers was already seen and at 21 DPO the amount of RFP+ non-vascular cells had also declined in controls (consistent with the transient nature of this avascular cell subset). We found that SOX2 was expressed in 42% of avascular RFP+ cells (Figure 3E, pie diagram). Thus, it is apparent that *Sox2*-loss in *Nestin*::creER2, R26-RFP, Sox2$^{fl/fl}$ animals affected a much larger population of traced cells than only the fraction of cells initially characterized as SOX2 positive. In particular, SOX2+ TAMEP were necessary for generating the entire population of traced avascular, myeloid-like cells. As SOX2+ TAMEP were the source for all TAMEP they are hereafter referred to as TAMEP progenitors.

Interestingly, we also noted that in addition to homozygous Sox2-knockouts (see above), even loss of a single Sox2-allele (*Nestin*::creER2, R26-RFP, Sox2$^{fl/WT}$) profoundly reduced TAMEP-numbers at 14DPO (Figure 3F) showing that TAMEP are haploinsufficient for *Sox2*. *Sox2*-haploinsufficiency is well described for some cell subsets, e.g., cells of the cochlea (Atkinson et al., 2018), while NPC or OPC remain fully functional with a single Sox2 allele (Mich et al., 2014; Zhao et al., 2015). Using mouse models (Arnold et al., 2011; Riccardi et al., 2016), tracing cells with a single (*Sox2*::creER2, R26-RFP) or with two functional copies (*Sox2*::IRES-creER2, R26-RFP) of Sox2, we find that TAMEP were traced exclusively with the *Sox2*::IRES-creER2, R26-RFP model (Figure 3F). Crossbreeding of *Sox2*::-IRES-creER2, R26-RFP mice with *Cx3cr1*-GFP strain (Jung et al., 2000) corroborated that traced cells in this model had a myeloid appearance (Figure 3G); of note, the *Sox2*::IRES-creER2, R26-RFP model did not immunolabel for PDGFRB, which confirmed that pericytes did not derive from TAMEP. Overall, we traced TAMEP from two independent mouse models and found that TAMEP are haploinsufficient for SOX2, distinguishing TAMEP from astrocytes, OPC, or NPC, which show no *Sox2*-gene dosage effects.

TAMEP do not derive from peripheral or CNS macrophages

We investigated if TAMEP (and/or their progenitors) may be derived from the hematopoietic system. To do this, we

(E) Confocal maximum projection for Iba1 and F4/80 at 7 DPO (Nes-RFP model); note that traced cells express F4/80 but not Iba1 (orthogonal view).
(F) Intratumoral avascular RFP+ cells (Nes-RFP model) were analyzed by FACS; immune-positivity for CD11b was detected (representative data of 9 independent FACS experiments).
Data (in B) are presented as mean ± SD. Scale bars are 15 μm. See also Figure S3.

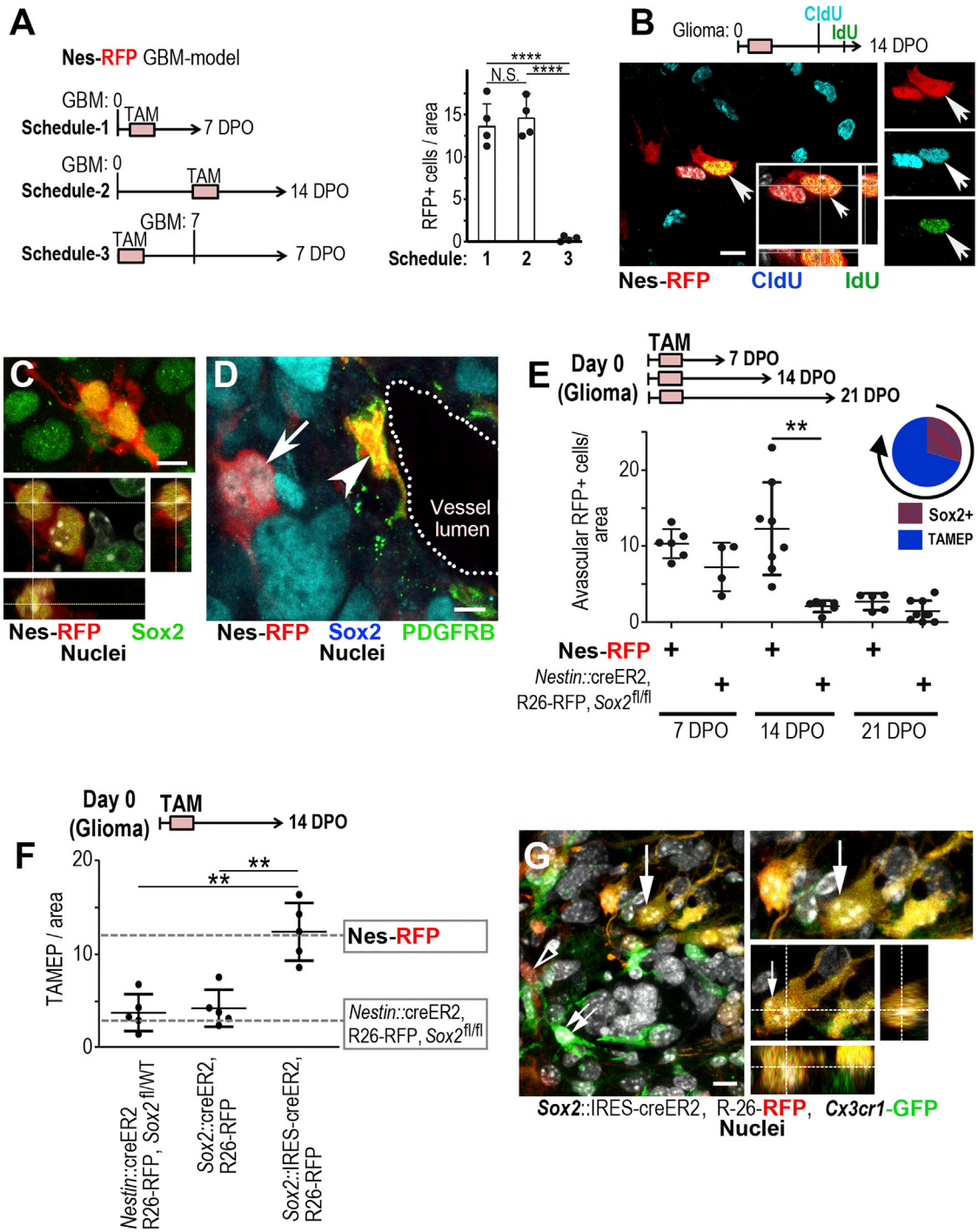

Figure 3. TAMEP are generated by a SOX2-dependent progenitor

(A) Different experimental schedules in Nes-RFP mice (each group: n = 4 animals); avascular RFP+ cells were only traced from tumor-bearing brains.

(B) CldU/IdU uptake inspected by immunofluorescence (arrow indicates one identical cell) at 14DPO (see schedule; n = 8 Nes-RFP mice).

(C and D) (C) Robust SOX2 expression in a set of avascular traced cells (maximum projection; orthogonal view) in the Nes-RFP glioma model was (D) restricted to the avascular cell population (arrow); absent from traced (PDGFRB+) perivascular cells (arrowhead).

(E) Quantification of avascular RFP+ cells in GBM of Nes-RFP mice or conditional *Sox2*-knockouts: *Sox2*-knockout strongly reduced avascular traced cells at 14 DPO; pie diagram: SOX2 is expressed in 42% of avascular RFP+ cells and SOX2-loss abrogates the vast majority of TAMEP; hence, Sox2+ TAMEP progenitors are necessary for the generation of TAMEP (arrow); each dot indicates data from one mouse; with n = 4 to n = 8 animals per experimental group.

(legend continued on next page)

generated bone-marrow chimeric models, in which lethally irradiated Nes-RFP mice received bone marrow from the *Spi1*-GFP strain (Back et al., 2005), abbreviated as chimera-1. The *Spi*1-gene encodes the transcription factor PU.1, which is essential for establishing the myeloid lineage and some other lymphocytes (Back et al., 2005). Also, we transplanted bone marrow from Nes-RFP animals into wild-type mice (chimera-2). After established bone-marrow reconstitution, mice were orthotopically inoculated with glioma, and cell-tracing was initiated by tamoxifen-application (scheme in Figure 4A). Non-irradiated Nes-RFP mice were used as controls. As expected, in chimera-1, we observed a massive accumulation of bone-marrow-derived *Spi1*-GFP+ cells in GBM, and brain-endogenous Nes-RFP+ cells remained at control levels (Figures 4A and 4B). However, no intracranial accumulation of bone-marrow transplanted Nes-RFP+ cells was observed in chimera-2 (Figures 4A and 4B). Intratumoral traced cells of the Nes-RFP strain never expressed the pan-leukocyte marker CD45 (Figure 4C) or the monocyte-marker CCR2 (Figure 4D), as investigated with Nes-RFP, CCR2-GFP transgenic mice (Bowman et al., 2016; Chen et al., 2017). The *Flt3*-cre mouse line containing a GFP-reporter for lineage tracing from bone-marrow stem cells (Benz et al., 2008) was used as a glioma model and revealed that SOX2 was absent from bone-marrow-derived cells (Figure 4E). Finally, we also tested a microglia-origin of TAMEP by using the *Cx3cr1*::creER, R26-RFP model, which accurately identifies microglia (and other CNS-resident macrophages) after adequate tamoxifen pulse/chase schedules (Huang et al., 2018; Wieghofer et al., 2015). This showed that cells of the microglia lineage never expressed Sox2 (Figure 4F), thereby excluding that TAMEP progenitors (and subsequently TAMEP) stem from brain macrophages. All in all, we used a range of models identifying blood-borne macrophages or microglia as well as other CNS-resident phagocytes and consistently observed that TAMEP do not relate to established sets of myeloid cells (Figure 4G).

Identification of TAMEP in human GBM

Hitherto, we relied on transgenic mouse models with orthotopic implantation of glioma cells to identify TAMEP. In order to extend our study to different models and human brain tumor biopsies, we sought to establish scRNA-seq profiles as well as immunohistochemical procedures to locate TAMEP in human material. We have shown that TAMEP and their progenitors express myeloid markers (without belonging to the myeloid lineage) and require SOX2 (in order to maintain their own lineage). Our previous experiments demonstrated that SOX2 is absent from blood-borne myeloid cells or tissue macrophages (Figures 4E–4G), which is in full agreement with other reports (Liu et al., 2018; Rosager et al., 2017; Sarkar et al., 2014). However, TAMEP expressing the myeloid marker CX3CR1 derive from SOX2-positive progenitors (Figure 3G). Therefore, we investigated if SOX2 and CX3CR1 coexpressing TAMEP would be observed in our scRNA-seq data from lineage-traced intratumoral cells. This was indeed the case, we detected RFP+, CX3CR1/SOX2-coexpressing TAMEP (Figures 5A and S4A), which have similarity with microglia (Figure S4B). Immunofluorescence inspection corroborated that Nes-RFP, *Cx3cr1*-GFP+ transgenic mice express SOX2 (Figure 5B).

Combinatorial detection of (nuclear) transcription factors represents a very reliable way for cell identification, and hence, we asked if some TAMEP also express the (essential) myeloid transcription factor *Spi1*/PU.1 (Back et al., 2005). Therefore, we first investigated if PU.1 was expressed in GBM-parenchymal cells traced with the *Sox2*::IRES-creER2, R26-RFP model and confirmed PU.1 in *Sox2*-traced cells (Figure 5C). Second, we determined if Nes-RFP, *Spi1*-GFP mice (reporting PU.1-expression as GFP-signal) would express SOX2, which was also the case (Figure 5D). We found that SOX2 immuno-positivity in myeloid-reporter strains (*Cx3cr1*-GFP or *Spi1*-GFP) was exclusively observed in cells coexpressing RFP (from the Nes-RFP strain). Hence, SOX2-expression in myeloid marker positive cells in our models was restricted to TAMEP and combinatorial immuno-detection of SOX2 and PU.1 or CX3CR1 represents a useful strategy to identify TAMEP in human material since SOX2/PU.1 coexpression is otherwise only seen in some forms of leukemia (Tosic et al., 2018).

These defining features for TAMEP from transgenic mouse models (data from immunofluorescence analysis and from scRNA-seq data identifying TAMEP) were now applied to human GBM-derived datasets. We analyzed scRNA-seq datasets from CD45+ GBM-associated cells (Sankowski et al., 2019) and from samples without enrichment for specific cell types (Wang et al., 2019). Coherent with our previous finding that TAMEP are CD45 negative (Figure 4C), we did not find any SOX2+/SPI1+ double-positive cells in CD45+ GBM-derived cells, while we detected SOX2+/SPI1+ double-positive cells in three out of five GBM samples obtained without CD45-targeting purification (Figure S4C). Regional abundance (or scarcity) of TAMEP (subsequently observed by immunofluorescence, as described below) may explain why two biopsies did not contain SOX2+/SPI1+ cells. Detailed transcriptome information was then obtained from the dataset with the best coverage (SF11644 in Figure S4C). We observed that cells with a myeloid expression profile from this sample were segregated into 4 clusters (Figure 5E) and that SOX2+/SPI1+ cells were significantly enriched in cluster 2 (chi^2-test: OR = 16.96, $p < 10^{-16}$). A machine-learning approach (Malta et al., 2018) named one-class logistic regression (OCLR) allowed to score patient-derived expression profiles for their overall similarity with mouse TAMEP scRNA-seq data. This indicated that cells in cluster 2 have a higher TAMEP index than other clusters. In agreement with our TAMEP profile, cluster 2 was enriched for cells that express the OPC marker PDGFRA and for CX3CR1. It cannot be formally excluded that multiplets contribute to expression profiles of datasets from microfluidics

(F) Ablation of one *Sox2*-allele was sufficient to reduce TAMEP-numbers (comparable to *Sox2*-knockouts; lower dashed line); the *Sox2*::creER2 strain (with one functional *Sox2*-allele) did not trace TAMEP; the *Sox2*::IRES-creER2 strain (containing two functional Sox2 alleles) traced TAMEP (comparable to Nes-RFP controls; upper dashed line; n = 5 mice per experimental group).

(G) *Sox2*::IRES-creER2, R26-RFP, *Cx3cr1*-GFP glioma models were used to trace TAMEP (arrow); single-positive cells (GFP+; double-arrow) or RFP+ (bi-color arrowhead) are also shown. Each value (in E and F) represents one mouse, data (in A, E, and F) are presented as mean ± SD; statistical significance (in A, E, and F) was tested by one-way ANOVA with post hoc test and is indicated: (N.S., non-significant; **$p < 0.01$; ****$p < 0.001$); scale bars are 5 μm.

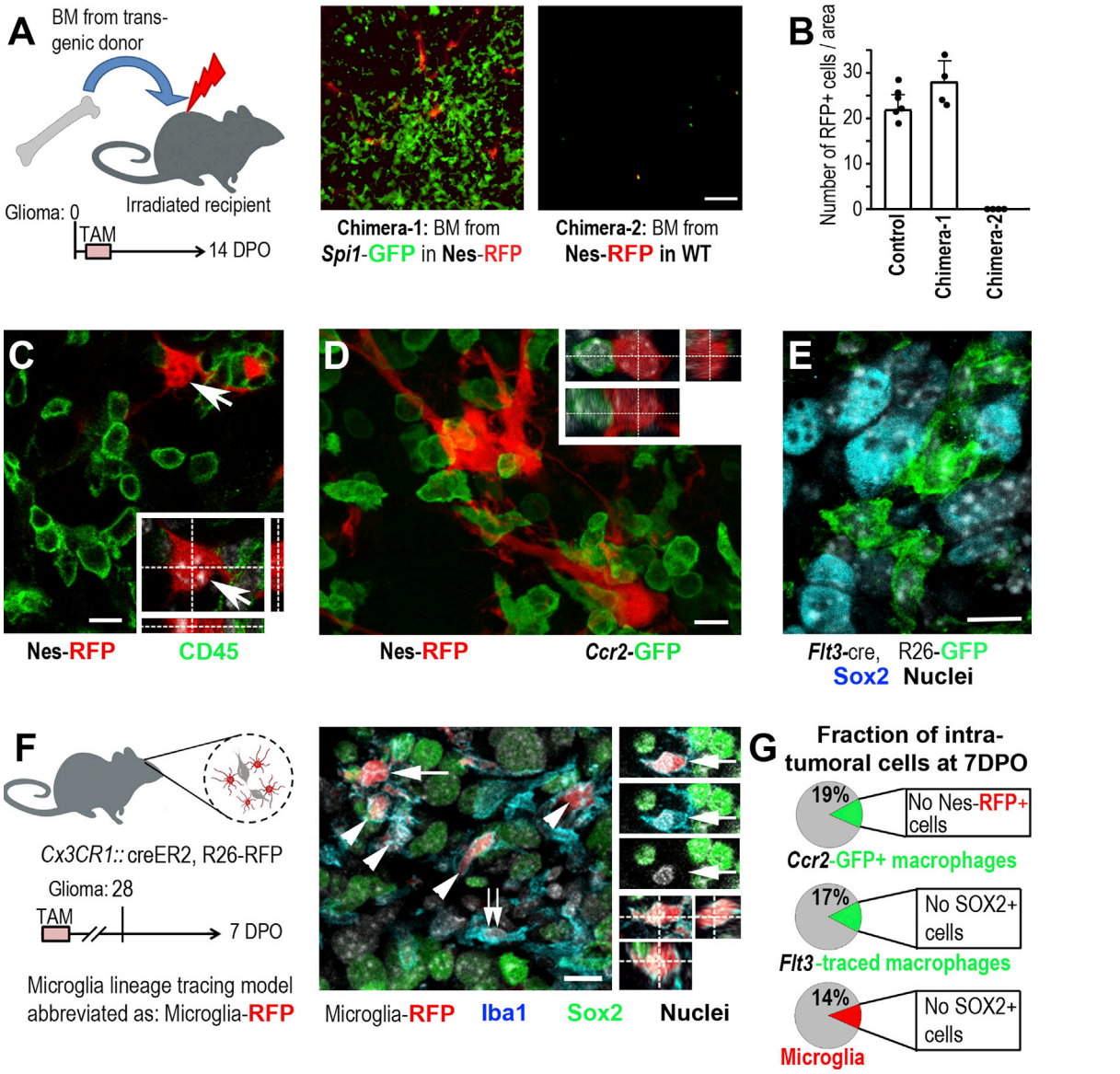

Figure 4. TAMEP and their progenitors do not derive from the myeloid lineage

(A) Lineage tracing in bone marrow (BM) chimeric models at 14DPO, chimera-1: Nes-RFP mice received BM from *Spi1*-GFP mice. Chimera-2: wild-type mice obtained BM from Nes-RFP mice.

(B) BM-transfer was successful (GFP+ cells in glioma of chimera-1, n = 4 mice); BM-derived RFP+ cells had no tropism to GBM (chimera-2; n = 4 mice); controls (without BM-exchange; n = 6 mice).

(C) RFP+ avascular cells do not express CD45.

(D) The Nes-RFP, *Ccr2*-GFP glioma-bearing mice contained no GFP+/RFP+ cells.

(E) *Flt3*-cre traced cells (GFP+) in gliomas never express SOX2.

(F) A pulse-chase paradigm in a *Cx3cr1*::creER, R26-RFP model excluded SOX2-expression from traced glioma-associated microglia (RFP+ cells; arrow); staining for Iba1 in microglia (arrowheads) and macrophages (double-arrow).

(G) Nes-RFP+ or Sox2+ cells never overlapped with macrophages (*Ccr2*-GFP+), did not derive from BM stem cells (*Flt3*-traced) and did not origin from microglia. Data (in B) are presented as mean ± SD; statistical significance was tested by one-way ANOVA with post hoc test and is indicated: *p < 0.05, ****p < 0.0001); scale bars are 50 μm in (A), 10 μm in (C), (D) and (E).

(human GBM). However, expression profiles for mouse TAMEP (clearly excluding multiplets by flow cytometry) served to identify human TAMEP with high reliability. Altogether, this underscores the validity of our approach for TAMEP detection in samples from human GBM.

The bioinformatics identification of TAMEP in mouse and human GBM was substantiated by immunofluorescence inspection of TAMEP in GBM models and human GBM specimen. First, we used a genetic GBM mouse model (Figures S5A and S5B) and explored immunofluorescence for SOX2 and PU.1. We

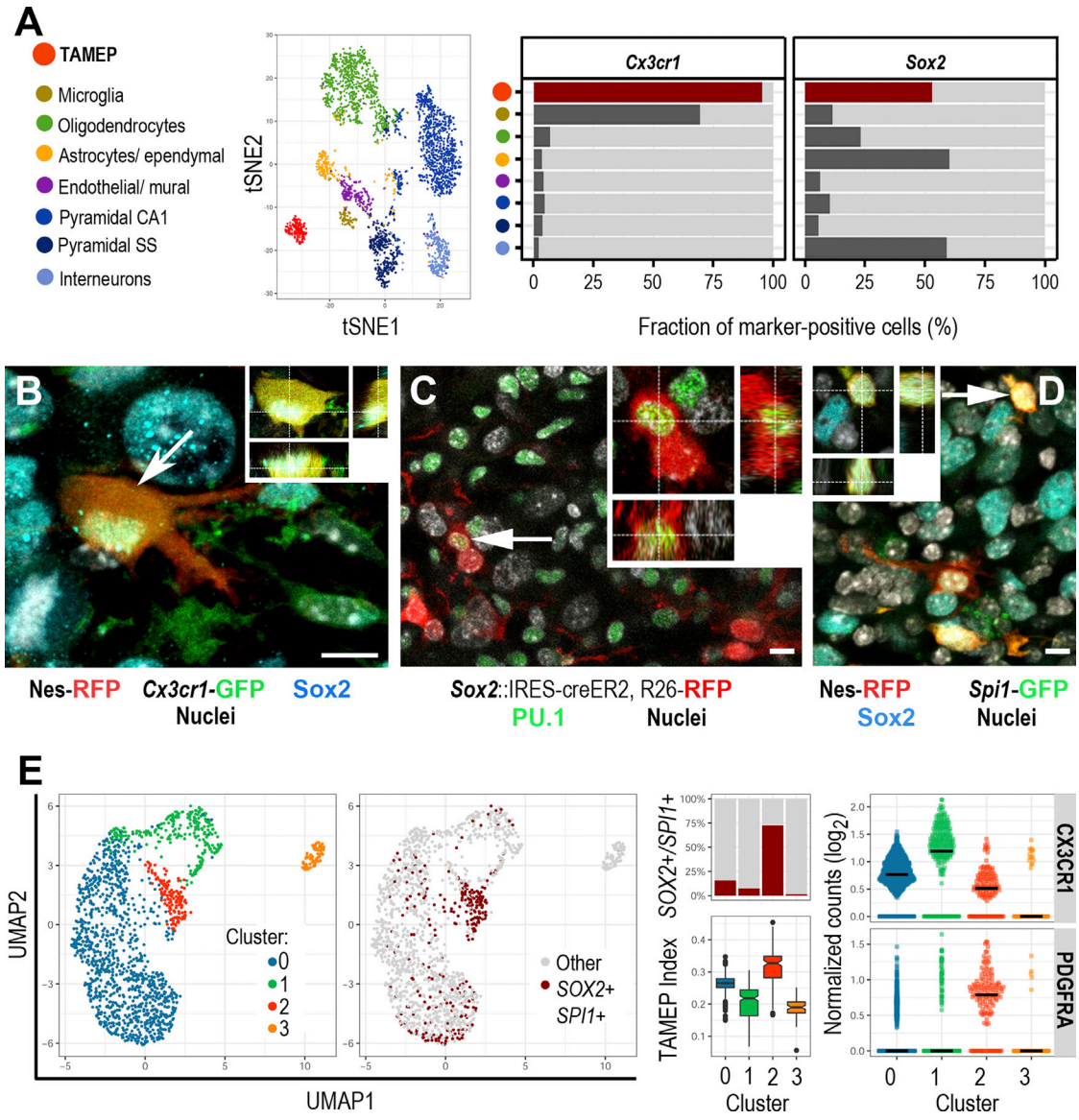

Figure 5. TAMEP are observed in murine and human GBM

(A) Nes-RFP cells were purified from experimental gliomas and scRNA-seq data (TAMEP), compared with established single-cell expression profiles of identified brain cells after unsupervised clustering and presented as tSNE-plot; expression levels for Cx3cr1 and Sox2 were quantified in all cell populations.

(B) SOX2 and GFP colabel exclusively in avascular RFP+ cells in glioma-bearing Nes-RFP, *Cx3cr1*-GFP models.

(C) Immunofluorescence for PU.1 in tumor-associated RFP+ cells from the *Sox2*::IRES-creER2, R26-RFP model (arrow).

(D) Sox2-immunolabeling is restricted to traced avascular cells in Nes-RFP, *Spi1*-GFP transgenic mice.

(E) scRNAseq data from 3/5 human GBM-datasets indicated abundance of TAMEP. One dataset was inspected in detail for tumor-associated myeloid cells and a UMAP-plot indicated 4 different myeloid clusters; *SOX2+/SPI1+* cells are enriched in cluster 2. A large TAMEP-defining gene set was obtained from mouse transgenic models and the same set of genes identified TAMEP in cluster-2 of human GBM by a OCLR model (TAMEP index). Expression pattern for *CX3CR1* and *PDGFRA* recapitulate the expectations for TAMEP in human GBM. Scale bars represent 5 μm (B-D). See also Figure S4.

found Sox2 single-positive nuclei (Figure 6A) indicating glioma cells, PU.1 single-positive nuclei (representing tumor-associated myeloid cells), and areas with many SOX2/PU.1 double-positive nuclei indicating a loco-regional abundance of TAMEP. TAMEP were reliably detected in GBM but were absent from mouse models for stroke or neuro-inflammation (Figures S5D–S5K) as quantified in Figure 6B. SOX2/PU.1 coexpressing cells were locally abundant (with regional heterogeneity) in a range of human CNS neoplasms comprising GBM and additional othotopic models (Figures 6C–6E and S6A–S6D), whereas SOX2/PU.1 double-positive cells were absent from tumor-free human brain (Table S3). Altogether, we were able to consistently identify cells expressing the combinatorial TAMEP markers SOX2+/SPI1+ or PDGFRA/CX3CR1 in multiple human GBMs and identified a

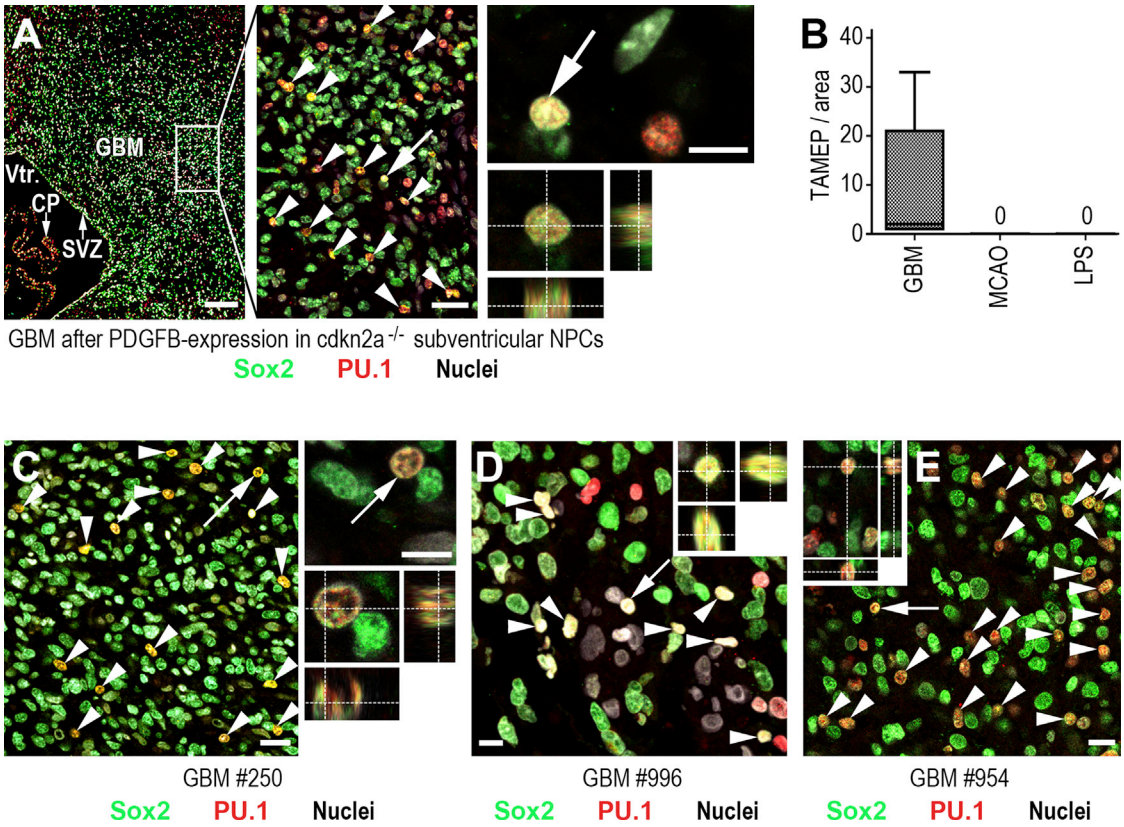

Figure 6. Confirmation of TAMEP in human and mouse transgenic GBM

(A) Regional abundance of TAMEP (SOX2+/PU.1+; arrowheads) in a genetic glioma model (arrow; magnified).

(B) Quantification of TAMEP after middle cerebral artery occlusion (MCAO), LPS (i.c.) or in GBM (n = 4 mice per group in all cases; box and whisker plot).

(C–D) TAMEP (arrowheads) in biopsies from human GBM; magnified in orthogonal view (arrows). Scale bars are 200 μm (A), 30 μm (in magnified part of A), 10 μm (insert in A), and 30 μm (C–E). See also Figures S5 and S6.

population of cells in one human GBM whose transcriptional profile showed a high TAMEP-score. These data suggest that TAMEP are present in human GBMs.

TAMEP shape GBM angiogenesis

Next, we asked if TAMEP and their progenitors have a particular pathological role in GBM. In *Nestin*::creER2, R26-RFP, *Sox2*$^{fl/fl}$ mice (Sox2-KO; Figures 7A–7C and S7A–S7G), we observed morphological changes in tumor vessels (as compared with *Sox2* wild-type controls; WT) and therefore quantified the extent of GBM vascularization in Nes-RFP or *Sox*-deficient mice over a time course (Figure 7A). At earlier time points (7 and 14 DPO; Figure S7H), we noted a reduction in vessel branch-points after conditional *Sox2*-loss, in comparison with controls, and this effect persisted into advanced glioma stages (Figure 7B). Intratumoral vascularization was strongly reduced at 21DPO in *Nestin*::creER2, R26-RFP, *Sox2*$^{fl/fl}$ mice (and in *Nestin*::creER2, R26-RFP, *Sox2*$^{fl/WT}$ models; Figure S7A), as compared with *Sox2*-WT mice. Furthermore, we included an additional control and ablated the entire population of traced cells by conditional expression of diphtheria toxin-A (*Nestin*::creER2, R26-RFP, R26-iDTA; abbreviated as iDTA in Figure 7B), which did not mediate any additive effects with respect to the extent of tumor vascularization in comparison with conditional *Sox2*-KO models. However, conditional *Sox2*-loss affected vessel-morphology generating vessels with a very large lumen and little complexity (this was rare in controls; Figures 7C and S7B–S7G). The vascular cavities in gliomas from the *Sox2*-knockout model lacked full pericyte coverage (Figure 7C). We investigated a potential reciprocal connection between TAMEP and tumor vessels by determining if anti-angiogeneis can reduce TAMEP density, but this was not the case (Figure S7I). Overall, this revealed that TAMEP (and their progenitors) have a strong impact on GBM vascularization and can persistently modulate the intratumoral vascular network.

TAMEP affect GBM expansion

GBM growth is supported by tumor vascularization (Jain et al., 2007) and reduced tumor vessel density (as seen after TAMEP-reduction) should impact on GBM expansion (Mastrella et al., 2019; von Baumgarten et al., 2011). In order to investigate this point, we used our established mouse models that produce diminished TAMEP cell numbers (*nestin*::creER2, R26-RFP, *Sox2*$^{fl/fl}$ or *nestin*::creER2, R26-RFP, *Sox2*$^{fl/WT}$), ablating TAMEP plus intratumoral pericytes (*nestin*::creER2, R26-RFP, R26-iDTA) or controls (Nes-RFP; leaving TAMEP intact). After implanting GBM and stimulation with tamoxifen (Figure 7D), we determined GBM volumes (Figures 7E and 7F) by histological inspection of

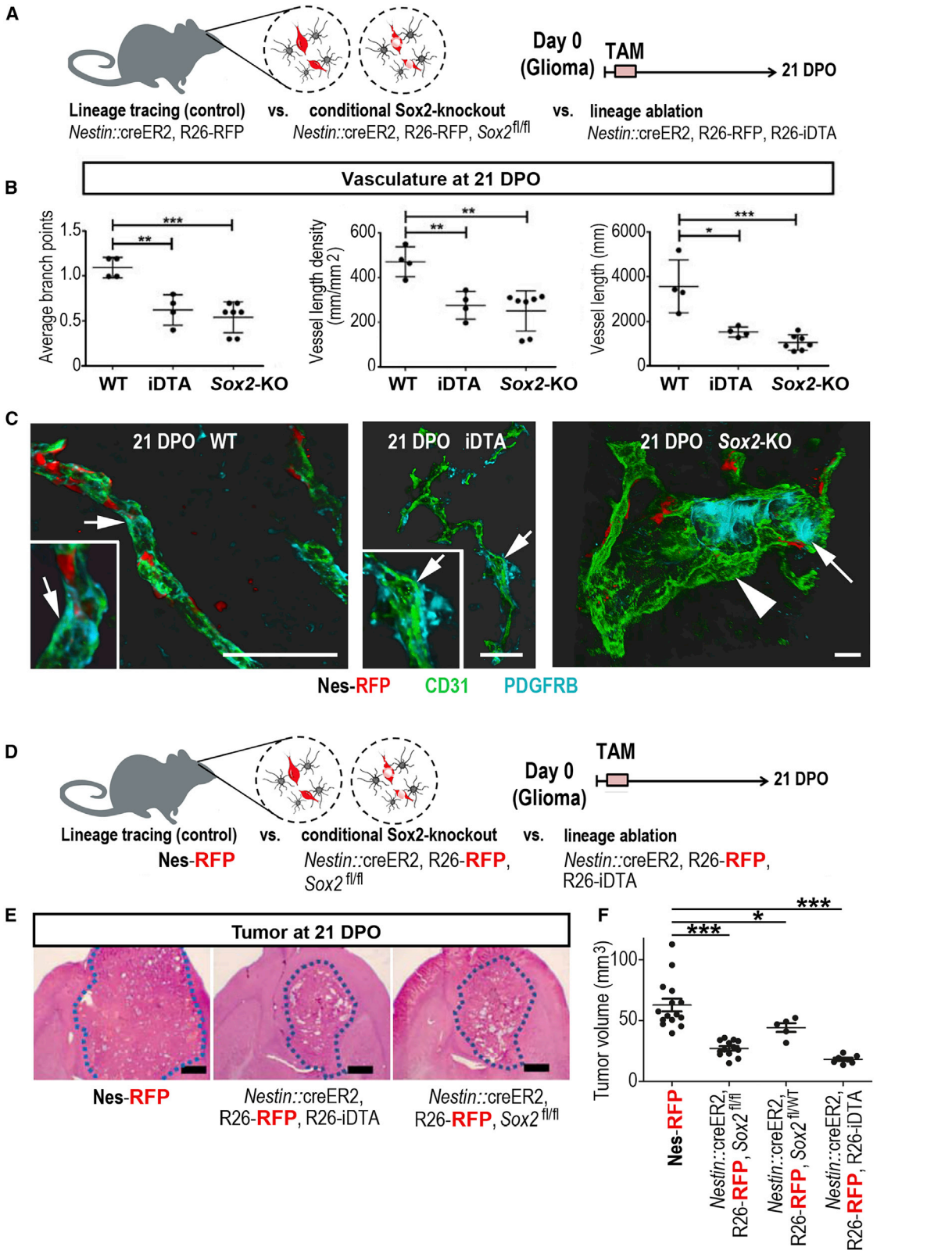

(legend on next page)

brain serial sections. In agreement with the role of TAMEP in GBM vascularization, we found that numbers of TAMEP (or TAMEP plus pericytes) largely reduced GBM volumes (Figure 7F). This effect was TAMEP-specific as heterozygosity for *Sox2* already modulated tumor expansion and as *Sox2*-conditional knockout in endothelia, pericytes or microglia of GBM-models did not reduce the tumor-size (Figure S7J). In summary, our work introduces TAMEP as a GBM-parenchymal component with high pathological impact.

DISCUSSION

We described a progenitor cell type of the brain tumor microenvironment, termed TAMEP-progenitor, which has a profound role in neoplastic angiogenesis in the brain. These progenitors were initially characterized by expression of the stem-cell-related transcription factor SOX2 (Sarkar and Hochedlinger, 2013) and by an active transgenic *Nestin* gene-promoter serving as a marker for immature cells (Bernal and Arranz, 2018). TAMEP progenitors were specifically ablated by conditional *Sox2*-knockout, preventing the intratumoral accumulation of TAMEP. Also, we discovered that TAMEP progenitors are sensitive to alterations in *Sox2* gene-dosage, which served as a criterion for additional TAMEP tracing models corroborating our findings from Nes-RFP mice. Our scRNA-seq data indicated an aberrant, myeloid-like expression profile in TAMEP. This was subsequently validated in different models by transgenic reporters and immunofluorescence markers, e.g., PU.1, CD11b, F4/80, or CX3CR1 (Back et al., 2005; Glass and Synowitz, 2014). However, despite this myeloid appearance, we could clearly show that TAMEP are not myeloid cells: we excluded that TAMEP (or their progenitors) derive from hematopoietic niches in the bone marrow (using mouse-chimera, *CCR2*-reporters, or *Flt3*-based tracing), and we ruled out that TAMEP derive from microglia using the Cx3cr1-creER2 model (Benz et al., 2008; Chen et al., 2017; Wieghofer et al., 2015). A non-myeloid origin for TAMEP is also supported by the notion that these cells are generated from a (*Sox2*-dependent) progenitor, which excludes a microglial source (Huang et al., 2018). All in all, this supports the view that tumor-associated myeloid cells are highly heterogeneous (Audia et al., 2017; Glass and Synowitz, 2014; Hambardzumyan et al., 2016) and even bear non-myeloid subsets disguised as a myeloid component.

TAMEP progenitors are different from established, GBM-associated stem and progenitor cell types, such as MSC, OPC, or NPC, as observed by intravital imaging, immunofluorescence studies in different transgenic lineage-tracing models, or pathological outcome in lineage-ablation experiments. The most prominent sources for MSC include the vascular mural compartment (Crisan et al., 2008) or the bone marrow (Frenette et al., 2013), but these were experimentally excluded for TAMEP. In addition, MSC markers (Jones and Schäfer, 2015) were absent from TAMEP. OPCs (which are not vessel associated) contribute to GBM expansion by generating mural cells of the intratumoral vasculature (Huang et al., 2014), but such a contribution was again ruled out by intravital imaging. NPC have a strong GBM tropism only in the young brain but not in the age range of mice used in our study (Stock et al., 2012; Walzlein et al., 2008). Furthermore, NPCs exert anti-tumor effects in young mice (Stock et al., 2012), whereas TAMEP support glioma expansion. Sox2-based tracing of TAMEP requires models (Riccardi et al., 2016) that are different from lineage-tracing models for NPC or OPC (Mich et al., 2014; Zhao et al., 2015), as progenitors for TAMEP are Sox2-haploinsufficient (whereas NPC/OPC are not). These features clearly distinguish TAMEP progenitors from other known progenitors within the GBM parenchyma.

We show that a small and distinct population of cells with a myeloid expression profile has a specific impact on brain neoangiogenesis. A role for myeloid cells in GBM angiogenesis was previously observed (Brandenburg et al., 2016; Mathivet et al., 2017). Reducing the numbers of monocyte-derived macrophages was exploited to improve chemotherapy but had no direct tumor-suppressing effect (Mathivet et al., 2017). In contrast, CNS-specific ablation of CD11b-positive cells resulted in an overall reduction in intratumoral vessels and glioma size (Brandenburg et al., 2016). Hence, dissecting the set of CD11b-positive cells is interesting in order to establish strategies for direct anti-tumor effects. In this work, we explored one GBM-associated subpopulation of CD11b-positive cells (TAMEP) with striking angiogenic capacity. Altogether, the transient set of TAMEP is required for a dense and functional vascularization of GBM, thus offering a new and promising therapeutic target in neurooncology.

STAR★METHODS

Detailed methods are provided in the online version of this paper and include the following:

- KEY RESOURCES TABLE
- RESOURCE AVAILABILITY
  - Lead contact

Figure 7. TAMEP and their progenitors control glioma expansion

(A) Intratumoral vascularization was quantified in controls, *Sox2* conditional knockouts (*Sox2*-KO), or in a lineage-ablation model (iDTA) at 21 DPO.

(B) Parameters for vascular morphology like intratumoral vascular branching and vascular complexity are strongly modulated in *Sox2*-KO (n = 7 mice) with no additional effects in the iDTA model (n = 4) as compared with controls (n = 4).

(C) 3D-reconstruced intratumoral vessels with immunofluorescence for endothelia (CD31) and pericytes (PDGFRB); arrows correspond to magnified areas in WT (control) and iDTA models; specific ablation of TAMEP (*Sox2*-KO) generates enlarged vascular cavities with patchy association of pericytes (arrow) and pericyte-free areas (arrowhead).

(D) Orthotopic GBM were induced in Nes-RFP mice (controls), *Sox2* conditional knockouts, or in a lineage-ablation model, tamoxifen was applied and tumor size was quantified in all models at 21 DPO.

(E) Representative micrographs for GBM histopathology in three experimental models at 21 DPO; the cell-dense tumor mass is outlined.

(F) Quantification of GBM size in controls (Nes-RFP, n = 15), homozygous (n = 5) or heterozygous (n = 13) *Sox2*-ablation in Nes-RFP and iDTA strains (n = 6). Data (in B and F) are presented as mean ± SD; statistical significance according to one-way ANOVA with post hoc test is indicated: $^{**}p < 0.01$, $^{****}p < 0.0001$. Each dot (in the diagrams) represents the average statistical value obtained from one mouse. Scale bars are 100 μm (C) or 1mm (E). See also Figure S7.

- Materials availability
- Data and code availability
- EXPERIMENTAL MODEL AND SUBJECT DETAILS
  - Mice
  - Human glioblastoma specimens
  - Cell culture
- METHOD DETAILS
  - Tumor inoculation and tamoxifen treatment
  - Generation of mouse bone marrow chimeras
  - *In-vivo* multiphoton laser scanning microscopy
  - Temporary middle cerebral artery occlusion (tMCAo) as ischemic injury
  - LPS treatment
  - Genetically induced GBM
  - Administration of thymidine analogs
  - Histology and immunohistochemistry
  - Microscopy, image-processing and quantification
  - Tumor size quantification
  - Stereological analysis of vasculature
  - Single cell preparation and staining for flow cytometry
  - Fluorescence activated cell sorting
  - Single-cell RNA-Seq data generation
  - Single-cell RNA-Seq data processing
  - Human single cell data processing
- QUANTIFICATION AND STATISTICAL ANALYSIS

SUPPLEMENTAL INFORMATION

Supplemental Information can be found online at https://doi.org/10.1016/j.cels.2021.01.002.

ACKNOWLEDGMENTS

R.G. and R.E.K. gratefully acknowledge funding by the "Anni-Hofmann Stiftung," the DFG (GL691/2; SFB824), and the "Wilhelm Sander Stiftung." L.C., Y.L., W.Z., X.W., and D.Z. were supported by the "China Scholarship Council" (CSC) graduate scholarships and K.E. by the LMU FöFoLe program. C.G. was funded by "the Swiss Cancer League" (KLS-4518-08-2018). E.M. was supported by DFG (MO2562/1-2) and L.v.B. by the "Else Kröner Fresenius Stiftung (A265)" and the "Bayerische Gleichstellungsförderung." C.S. was supported by the DFG (SFB914) and the DZHK and BMBF. W.E., I.H., and P.J. were supported by LMUexcellent SFB1243. Furthermore, we are grateful to the Core Facility Bioimaging at the Biomedical Center and the animal facilities at the University Clinics Munich. PU.1kiGFP mice were provided by Dr. Philippe Kastner (IGBMC - CNRS UMR 7104), *Ve-cadherin*-creER2 mice by Ralf Adams (MPI Mol. Biomedicine), and Sox2-IRES-creER2 mice by the Novartis Institutes of BioMedical Research. We thank Christoph Ziegenhain for scRNA-seq library generation, Magali Soumillon and Tarjei Mikkelsen for the SCRB-seq protocol, Stefan Krebs and Helmut Blum from the LAFUGA platform (LMU) for sequencing, and Aaron Diaz (UCSF) for sharing scRNA-seq data.

AUTHOR CONTRIBUTIONS

R.E.K., M.Synowitz, L.v.B., C.S., W.E., E.M., and R.G. designed experiments; R.E.K., L.C., Y.L., D.Z., H.Z., J.C., W.Z., Y.W., K.E., L.S., P.J., I.H., F.M., C.F., M.H., S.V.K., S.S., M.S., I.A., E.M., L.v.B., C.S., W.E., and R.G. conducted experiments and analyzed data. P.J. analyzed human scRNA-seq datasets. R.E.K., Y.L., Y.W., K.E., J.C.T., M. Schiemann, I.A., C.G., V.T., M. Synowitz, E.M., and R.G. obtained and characterized experimental models, generated the mouse model or provided scientific support. R.G. wrote the manuscript. All authors discussed the results and revised the manuscript text.

DECLARATION OF INTERESTS

The authors declare no competing interests.

Received: September 26, 2019
Revised: April 7, 2020
Accepted: January 4, 2021
Published: February 15, 2021

REFERENCES

Aldape, K., Brindle, K.M., Chesler, L., Chopra, R., Gajjar, A., Gilbert, M.R., Gottardo, N., Gutmann, D.H., Hargrave, D., Holland, E.C., et al. (2019). Challenges to curing primary brain tumours. Nat. Rev. Clin. Oncol. *16*, 509–520.

Aran, D., Looney, A.P., Liu, L., Wu, E., Fong, V., Hsu, A., Chak, S., Naikawadi, R.P., Wolters, P.J., Abate, A.R., et al. (2019). Reference-based analysis of lung single-cell sequencing reveals a transitional profibrotic macrophage. Nat. Immunol. *20*, 163–172.

Armulik, A., Genové, G., and Betsholtz, C. (2011). Pericytes: developmental, physiological, and pathological perspectives, problems, and promises. Dev. Cell *21*, 193–215.

Armulik, A., Genové, G., Mäe, M., Nisancioglu, M.H., Wallgard, E., Niaudet, C., He, L., Norlin, J., Lindblom, P., Strittmatter, K., et al. (2010). Pericytes regulate the blood-brain barrier. Nature *468*, 557–561.

Arnold, K., Sarkar, A., Yram, M.A., Polo, J.M., Bronson, R., Sengupta, S., Seandel, M., Geijsen, N., and Hochedlinger, K. (2011). Sox2(+) adult stem and progenitor cells are important for tissue regeneration and survival of mice. Cell Stem Cell *9*, 317–329.

Atkinson, P.J., Dong, Y., Gu, S., Liu, W., Najarro, E.H., Udagawa, T., and Cheng, A.G. (2018). Sox2 haploinsufficiency primes regeneration and Wnt responsiveness in the mouse cochlea. J. Clin. Invest. *128*, 1641–1656.

Audia, A., Conroy, S., Glass, R., and Bhat, K.P.L. (2017). The impact of the tumor microenvironment on the properties of glioma stem-like cells. Front. Oncol. *7*, 143.

Back, J., Allman, D., Chan, S., and Kastner, P. (2005). Visualizing PU.1 activity during hematopoiesis. Exp. Hematol. *33*, 395–402.

Behnan, J., Isakson, P., Joel, M., Cilio, C., Langmoen, I.A., Vik-Mo, E.O., and Badn, W. (2014). Recruited brain tumor-derived mesenchymal stem cells contribute to brain tumor progression. Stem Cells *32*, 1110–1123.

Benz, C., Martins, V.C., Radtke, F., and Bleul, C.C. (2008). The stream of precursors that colonizes the thymus proceeds selectively through the early T lineage precursor stage of T cell development. J. Exp. Med. *205*, 1187–1199.

Bernal, A., and Arranz, L. (2018). Nestin-expressing progenitor cells: function, identity and therapeutic implications. Cell. Mol. Life Sci. *75*, 2177–2195.

Binda, E., Visioli, A., Giani, F., Trivieri, N., Palumbo, O., Restelli, S., Dezi, F., Mazza, T., Fusilli, C., Legnani, F., et al. (2017). Wnt5a drives an invasive phenotype in human glioblastoma stem-like cells. Cancer Res. *77*, 996–1007.

Bondjers, C., He, L., Takemoto, M., Norlin, J., Asker, N., Hellström, M., Lindahl, P., and Betsholtz, C. (2006). Microarray analysis of blood microvessels from PDGF-B and PDGF-Rbeta mutant mice identifies novel markers for brain pericytes. FASEB J. *20*, 1703–1705.

Bowman, R.L., Klemm, F., Akkari, L., Pyonteck, S.M., Sevenich, L., Quail, D.F., Dhara, S., Simpson, K., Gardner, E.E., Iacobuzio-Donahue, C.A., et al. (2016). Macrophage ontogeny underlies differences in tumor-specific education in brain malignancies. Cell Rep. *17*, 2445–2459.

Brandenburg, S., Müller, A., Turkowski, K., Radev, Y.T., Rot, S., Schmidt, C., Bungert, A.D., Acker, G., Schorr, A., Hippe, A., et al. (2016). Resident microglia rather than peripheral macrophages promote vascularization in brain tumors and are source of alternative pro-angiogenic factors. Acta Neuropathol. *131*, 365–378.

Breiman, L. (2001). Random forests. Mach. Learn. *45*, 5–32.

Campos, B., Wan, F., Farhadi, M., Ernst, A., Zeppernick, F., Tagscherer, K.E., Ahmadi, R., Lohr, J., Dictus, C., Gdynia, G., et al. (2010). Differentiation therapy

exerts antitumor effects on stem-like glioma cells. Clin. Cancer Res. *16*, 2715–2728.

Chen, Z., Feng, X., Herting, C.J., Garcia, V.A., Nie, K., Pong, W.W., Rasmussen, R., Dwivedi, B., Seby, S., Wolf, S.A., et al. (2017). Cellular and molecular identity of tumor-associated macrophages in glioblastoma. Cancer Res. *77*, 2266–2278.

Crisan, M., Yap, S., Casteilla, L., Chen, C.W., Corselli, M., Park, T.S., Andriolo, G., Sun, B., Zheng, B., Zhang, L., et al. (2008). A perivascular origin for mesenchymal stem cells in multiple human organs. Cell Stem Cell *3*, 301–313.

Drachsler, M., Kleber, S., Mateos, A., Volk, K., Mohr, N., Chen, S., Cirovic, B., Tüttenberg, J., Gieffers, C., Sykora, J., et al. (2016). CD95 maintains stem cell-like and non-classical EMT programs in primary human glioblastoma cells. Cell Death Dis. *7*, e2209.

Frenette, P.S., Pinho, S., Lucas, D., and Scheiermann, C. (2013). Mesenchymal stem cell: keystone of the hematopoietic stem cell niche and a stepping-stone for regenerative medicine. Annu. Rev. Immunol. *31*, 285–316.

Giachino, C., and Taylor, V. (2009). Lineage analysis of quiescent regenerative stem cells in the adult brain by genetic labelling reveals spatially restricted neurogenic niches in the olfactory bulb. Eur. J. Neurosci. *30*, 9–24.

Glass, R., and Synowitz, M. (2014). CNS macrophages and peripheral myeloid cells in brain tumours. Acta Neuropathol. *128*, 347–362.

Goldmann, T., Wieghofer, P., Jordão, M.J., Prutek, F., Hagemeyer, N., Frenzel, K., Amann, L., Staszewski, O., Kierdorf, K., Krueger, M., et al. (2016). Origin, fate and dynamics of macrophages at central nervous system interfaces. Nat. Immunol. *17*, 797–805.

Goodpaster, T., and Randolph-Habecker, J. (2014). A flexible mouse-on-mouse immunohistochemical staining technique adaptable to biotin-free reagents, immunofluorescence, and multiple antibody staining. J. Histochem. Cytochem. *62*, 197–204.

Grathwohl, S.A., Kälin, R.E., Bolmont, T., Prokop, S., Winkelmann, G., Kaeser, S.A., Odenthal, J., Radde, R., Eldh, T., Gandy, S., et al. (2009). Formation and maintenance of Alzheimer's disease beta-amyloid plaques in the absence of microglia. Nat. Neurosci. *12*, 1361–1363.

Haghverdi, L., Lun, A.T.L., Morgan, M.D., and Marioni, J.C. (2018). Batch effects in single-cell RNA-sequencing data are corrected by matching mutual nearest neighbors. Nat. Biotechnol. *36*, 421–427.

Hambardzumyan, D., Gutmann, D.H., and Kettenmann, H. (2016). The role of microglia and macrophages in glioma maintenance and progression. Nat. Neurosci. *19*, 20–27.

Hammond, T.R., Robinton, D., and Stevens, B. (2018). Microglia and the brain: complementary partners in development and disease. Annu. Rev. Cell Dev. Biol. *34*, 523–544.

Ho, I.A., Toh, H.C., Ng, W.H., Teo, Y.L., Guo, C.M., Hui, K.M., and Lam, P.Y. (2013). Human bone marrow-derived mesenchymal stem cells suppress human glioma growth through inhibition of angiogenesis. Stem Cells *31*, 146–155.

Huang, Y., Hoffman, C., Rajappa, P., Kim, J.H., Hu, W., Huse, J., Tang, Z., Li, X., Weksler, B., Bromberg, J., et al. (2014). Oligodendrocyte progenitor cells promote neovascularization in glioma by disrupting the blood-brain barrier. Cancer Res. *74*, 1011–1021.

Huang, Y., Xu, Z., Xiong, S., Sun, F., Qin, G., Hu, G., Wang, J., Zhao, L., Liang, Y.-X., Wu, T., et al. (2018). Repopulated microglia are solely derived from the proliferation of residual microglia after acute depletion. Nat. Neurosci. *21*, 530–540.

Jain, R.K., di Tomaso, E., Duda, D.G., Loeffler, J.S., Sorensen, A.G., and Batchelor, T.T. (2007). Angiogenesis in brain tumours. Nat. Rev. Neurosci. *8*, 610–622.

Jones, E., and Schäfer, R. (2015). Where is the common ground between bone marrow mesenchymal stem/stromal cells from different donors and species? Stem Cell Res. Ther. *6*, 143.

Jung, S., Aliberti, J., Graemmel, P., Sunshine, M.J., Kreutzberg, G.W., Sher, A., and Littman, D.R. (2000). Analysis of fractalkine receptor CX(3)CR1 function by targeted deletion and green fluorescent protein reporter gene insertion. Mol. Cell. Biol. *20*, 4106–4114.

Kovacs, G.G. (2017). Cellular reactions of the central nervous system. Handb. Clin. Neurol. *145*, 13–23.

Krithje, J.H. (2015). T-distributed stochastic neighbor embedding using Barnes-hut implementation. J. Mach. Learn. Res. *9*, 2579–2605.

Lagace, D.C., Whitman, M.C., Noonan, M.A., Ables, J.L., DeCarolis, N.A., Arguello, A.A., Donovan, M.H., Fischer, S.J., Farnbauch, L.A., Beech, R.D., et al. (2007). Dynamic contribution of nestin-expressing stem cells to adult neurogenesis. J. Neurosci. *27*, 12623–12629.

Law, C.W., Chen, Y., Shi, W., and Smyth, G.K. (2014). voom: precision weights unlock linear model analysis tools for RNA-seq read counts. Genome Biol. *15*, R29.

Liu, Z., Kuang, W., Zhou, Q., and Zhang, Y. (2018). TGF-beta1 secreted by M2 phenotype macrophages enhances the stemness and migration of glioma cells via the SMAD2/3 signalling pathway. Int. J. Mol. Med. *42*, 3395–3403.

Llorens-Martín, M., and Trejo, J.L. (2011). Multiple birthdating analyses in adult neurogenesis: a line-up of the usual suspects. Front. Neurosci. *5*, 76.

Lun, A.T., McCarthy, D.J., and Marioni, J.C. (2016). A step-by-step workflow for low-level analysis of single-cell RNA-seq data with bioconductor. F1000Res. *5*, 2122.

Madisen, L., Zwingman, T.A., Sunkin, S.M., Oh, S.W., Zariwala, H.A., Gu, H., Ng, L.L., Palmiter, R.D., Hawrylycz, M.J., Jones, A.R., et al. (2010). A robust and high-throughput Cre reporting and characterization system for the whole mouse brain. Nat. Neurosci. *13*, 133–140.

Malta, T.M., Sokolov, A., Gentles, A.J., Burzykowski, T., Poisson, L., Weinstein, J.N., Kamińska, B., Huelsken, J., Omberg, L., Gevaert, O., et al. (2018). Machine learning identifies stemness features associated with oncogenic dedifferentiation. Cell *173*, 338–354.e15.

Mastrella, G., Hou, M., Li, M., Stoecklein, V.M., Zdouc, N., Volmar, M.N.M., Miletic, H., Reinhard, S., Herold-Mende, C.C., Kleber, S., et al. (2019). Targeting APLN/APLNR improves antiangiogenic efficiency and blunts proinvasive side effects of VEGFA/VEGFR2 blockade in glioblastoma. Cancer Res. *79*, 2298–2313.

Mathivet, T., Bouleti, C., Van Woensel, M., Stanchi, F., Verschuere, T., Phng, L.K., Dejaegher, J., Balcer, M., Matsumoto, K., Georgieva, P.B., et al. (2017). Dynamic stroma reorganization drives blood vessel dysmorphia during glioma growth. EMBO Mol. Med. *9*, 1629–1645.

Mich, J.K., Signer, R.A., Nakada, D., Pineda, A., Burgess, R.J., Vue, T.Y., Johnson, J.E., and Morrison, S.J. (2014). Prospective identification of functionally distinct stem cells and neurosphere-initiating cells in adult mouse forebrain. eLife *3*, e02669.

Mizutani, M., Pino, P.A., Saederup, N., Charo, I.F., Ransohoff, R.M., and Cardona, A.E. (2012). The fractalkine receptor but not CCR2 is present on microglia from embryonic development throughout adulthood. J. Immunol. *188*, 29–36.

Nutt, S.L., Metcalf, D., D'Amico, A., Polli, M., and Wu, L. (2005). Dynamic regulation of PU.1 expression in multipotent hematopoietic progenitors. J. Exp. Med. *201*, 221–231.

Parekh, S., Ziegenhain, C., Vieth, B., Enard, W., and Hellmann, I. (2018). zUMIs - a fast and flexible pipeline to process RNA sequencing data with UMIs. GigaScience *7*, giy059.

Prinz, M., Erny, D., and Hagemeyer, N. (2017). Ontogeny and homeostasis of CNS myeloid cells. Nat. Immunol. *18*, 385–392.

Riccardi, S., Bergling, S., Sigoillot, F., Beibel, M., Werner, A., Leighton-Davies, J., Knehr, J., Bouwmeester, T., Parker, C.N., Roma, G., and Kinzel, B. (2016). MiR-210 promotes sensory hair cell formation in the organ of corti. BMC Genomics *17*, 309.

Rosager, A.M., Sørensen, M.D., Dahlrot, R.H., Boldt, H.B., Hansen, S., Lathia, J.D., and Kristensen, B.W. (2017). Expression and prognostic value of JAM-A in gliomas. J. Neuro-Oncol. *135*, 107–117.

Sankowski, R., Böttcher, C., Masuda, T., Geirsdottir, L., Sagar, Sindram, E., Seredenina, T., Muhs, A., Scheiwe, C., Shah, M.J., et al. (2019). Mapping microglia states in the human brain through the integration of high-dimensional techniques. Nat. Neurosci. *22*, 2098–2110.

Sarkar, A., and Hochedlinger, K. (2013). The sox family of transcription factors: versatile regulators of stem and progenitor cell fate. Cell Stem Cell *12*, 15–30.

Sarkar, S., Döring, A., Zemp, F.J., Silva, C., Lun, X., Wang, X., Kelly, J., Hader, W., Hamilton, M., Mercier, P., et al. (2014). Therapeutic activation of macrophages and microglia to suppress brain tumor-initiating cells. Nat. Neurosci. *17*, 46–55.

Serrano, M., Lee, H., Chin, L., Cordon-Cardo, C., Beach, D., and DePinho, R.A. (1996). Role of the INK4a locus in tumor suppression and cell mortality. Cell *85*, 27–37.

Shaham, O., Smith, A.N., Robinson, M.L., Taketo, M.M., Lang, R.A., and Ashery-Padan, R. (2009). Pax6 is essential for lens fiber cell differentiation. Development *136*, 2567–2578.

Sörensen, I., Adams, R.H., and Gossler, A. (2009). DLL1-mediated Notch activation regulates endothelial identity in mouse fetal arteries. Blood *113*, 5680–5688.

Soumillon, M., Cacchiarelli, D., Semrau, S., van Oudenaarden, A., and Mikkelsen, T.S. (2014). Characterization of directed differentiation by high-throughput single-cell RNA-seq. biorxiv. https://doi.org/10.1101/003236.

Stock, K., Kumar, J., Synowitz, M., Petrosino, S., Imperatore, R., Smith, E.S.J., Wend, P., Purfürst, B., Nuber, U.A., Gurok, U., et al. (2012). Neural precursor cells induce cell death of high-grade astrocytomas through stimulation of TRPV1. Nat. Med. *18*, 1232–1238.

Stuart, T., Butler, A., Hoffman, P., Hafemeister, C., Papalexi, E., Mauck, W.M., 3rd, Hao, Y., Stoeckius, M., Smibert, P., and Satija, R. (2019). Comprehensive integration of single-cell data. Cell *177*, 1888–1902.e21.

Sun, M.Y., Yetman, M.J., Lee, T.C., Chen, Y., and Jankowsky, J.L. (2014). Specificity and efficiency of reporter expression in adult neural progenitors vary substantially among nestin-CreER(T2) lines. J. Comp. Neurol. *522*, 1191–1208.

Tosic, N., Petrovic, I., Grujicic, N.K., Davidovic, S., Virijevic, M., Vukovic, N.S., Pavlovic, S., and Stevanovic, M. (2018). Prognostic significance of SOX2, SOX3, SOX11, SOX14 and SOX18 gene expression in adult de novo acute myeloid leukemia. Leuk. Res. *67*, 32–38.

Van Hove, H., Martens, L., Scheyltjens, I., De Vlaminck, K., Pombo Antunes, A.R., De Prijck, S., Vandamme, N., De Schepper, S., Van Isterdael, G., Scott, C.L., et al. (2019). A single-cell atlas of mouse brain macrophages reveals unique transcriptional identities shaped by ontogeny and tissue environment. Nat. Neurosci. *22*, 1021–1035.

von Baumgarten, L., Brucker, D., Tirniceru, A., Kienast, Y., Grau, S., Burgold, S., Herms, J., and Winkler, F. (2011). Bevacizumab has differential and dose-dependent effects on glioma blood vessels and tumor cells. Clin. Cancer Res. *17*, 6192–6205.

Walzlein, J.H., Synowitz, M., Engels, B., Markovic, D.S., Gabrusiewicz, K., Nikolaev, E., Yoshikawa, K., Kaminska, B., Kempermann, G., Uckert, W., et al. (2008). The antitumorigenic response of neural precursors depends on subventricular proliferation and age. Stem Cells *26*, 2945–2954.

Wang, L., Babikir, H., Müller, S., Yagnik, G., Shamardani, K., Catalan, F., Kohanbash, G., Alvarado, B., Di Lullo, E., Kriegstein, A., et al. (2019). The phenotypes of proliferating glioblastoma cells reside on a single axis of variation. Cancer Discov. *9*, 1708–1719.

Wieghofer, P., Knobeloch, K.P., and Prinz, M. (2015). Genetic targeting of microglia. Glia *63*, 1–22.

Yu, G., and He, Q.Y. (2016). ReactomePA: an R/Bioconductor package for reactome pathway analysis and visualization. Mol. Biosyst. *12*, 477–479.

Zeisel, A., Muñoz-Manchado, A.B., Codeluppi, S., Lönnerberg, P., La Manno, G., Juréus, A., Marques, S., Munguba, H., He, L., Betsholtz, C., et al. (2015). Brain structure. Cell types in the mouse cortex and hippocampus revealed by single-cell RNA-seq. Science *347*, 1138–1142.

Zhang, Y., Chen, K., Sloan, S.A., Bennett, M.L., Scholze, A.R., O'Keeffe, S., Phatnani, H.P., Guarnieri, P., Caneda, C., Ruderisch, N., et al. (2014). An RNA-sequencing transcriptome and splicing database of glia, neurons, and vascular cells of the cerebral cortex. J. Neurosci. *34*, 11929–11947.

Zhao, C., Ma, D., Zawadzka, M., Fancy, S.P., Elis-Williams, L., Bouvier, G., Stockley, J.H., de Castro, G.M., Wang, B., Jacobs, S., et al. (2015). Sox2 sustains recruitment of oligodendrocyte progenitor cells following CNS demyelination and primes them for differentiation during remyelination. J. Neurosci. *35*, 11482–11499.

Ziegenhain, C., Vieth, B., Parekh, S., Reinius, B., Guillaumet-Adkins, A., Smets, M., Leonhardt, H., Heyn, H., Hellmann, I., and Enard, W. (2017). Comparative analysis of single-cell RNA sequencing methods. Mol. Cell *65*, 631–643.e4.

STAR★METHODS

KEY RESOURCES TABLE

REAGENT or RESOURCE	SOURCE	IDENTIFIER
Antibodies		
Rabbit anti-CD11b	Abcam	Cat#: ab52478; RRID: AB_868788
Rat anti- CD29	R&D Systems	Cat#: MAB2405; RRID: AB_2249264
Rat anti- CD31	Becton Dickinson	Cat#: 550274; RRID: AB_393571
Rat anti CD34	Abcam	Cat#: ab8158; RRID: AB_306316
Rat anti-CD44 [KM201]	Abcam	Cat#: ab25340; RRID: AB_470456
Rabbit anti CD45	Abcam	Cat#: ab10558; RRID: AB_442810
Mouse anti CD68	Abcam	Cat#: ab31630; RRID: AB_1141557
Rat anti- CD105	R&D Systems	Cat#: MAB1320; RRID: AB_2098896
Rabbit anti- CD146	Abcam	Cat#: ab75769; RRID: AB_2143375
Rabbit anti- CD 248	Thermo Fischer Scientific	Cat#: PA5-20436; RRID: AB_11154026
Rabbit anti- RFP	Abcam	Cat#: ab62341; RRID: AB_945213
Chicken anti- GFP	Aves	Cat#: GFP-1020; RRID: AB_10000240
Rabbit anti- Ki67	Abcam	Cat#: ab16667; RRID: AB_302459
Rat anti BrdU (IdU)	Serotec	Cat#: OBT0030; RRID: AB_609568
Mouse anti BrdU (CldU)	Becton Dickinson	Cat#: 347580; RRID: AB_10015219
Rabbit anti- von Willebrand Factor	Dako	Cat#: A0082; RRID: AB_2315602
Rat anti-F4/80 (BM8)	Santa Cruz	Cat#: Sc-52664; RRID: AB_629466
Goat anti Iba1	Abcam	Cat#: ab5076; RRID: AB_2224402
Rabbit anti Iba1	WAKO	Cat#: 019-19741; RRID: AB_839504
Goat anti- PDGFR-β	R&D Systems	Cat#: AF1042; RRID: AB_2162633
Rabbit anti- Desmin	Abcam	Cat#: ab15200; RRID: AB_301744
Rabbit anti NG2	Millipore	Cat#: AB5320; RRID: AB_11213678
Rat anti- Sca1	R&D Systems	Cat#: MAB1226; RRID: AB_2243980
Rat anti Sca1 / Ly6A/E	Abcam	Cat#: ab51317; RRID: AB_1640946
Mouse anti- Polysialic- Acid- NCAM 60	Millipore	Cat#: MAB 5324; RRID: AB_11210572
Goat anti Doublecortin	SantaCruz	Cat#: sc-271390; RRID: AB_10610966
Mouse anti Tuj1	Sigma	Cat#: T8578; RRID: AB_1841228
Mouse anti NeuN	Abcam	Cat#: ab104224; RRID: AB_10711040
Rabbit anti GFAP	Abcam	Cat#: ab7260; RRID: AB_305808
Mouse anti-S100ß	Sigma-Aldrich	Cat#: S2532; RRID: AB_477499
Mouse anti-CNpase	Abcam	Cat#: ab6319; RRID: AB_2082593
Rabbit anti Myelin Basic Protein	Abcam	Cat#: ab40390; RRID: AB_1141521
Rabbit anti-PU1/spi1_	Invitrogen	Cat#: A13971; RRID: AB_2534156
Rabbit anti-Sox 2	Abcam	Cat#: ab97959; RRID: AB_2341193
Goat anti-Sox 2	R&D Systems	Cat#: AF2018; RRID: AB_355110
Rabbit anti-Cre	Millipore	Cat#: 69050-3; RRID: AB_10806983
Biotynilated donkey anti mouse	Jackson Immuno Research	Cat#: 715-065-151; RRID: AB_2340785
Alexa 488 donkey anti rabbit	Jackson Immuno Research	Cat#: 711-545-152; RRID: AB_2313584
Alexa Fluor 594 donkey anti rabbit	Jackson Immuno Research	Cat#: 711-585-152; RRID: AB_2340621
Alexa Fluor 594 donkey anti rat	Jackson Immuno Research	Cat#: 712-585-150; RRID: AB_2340688
Alexa Fluor 594 donkey anti mouse	Jackson Immuno Research	Cat#: 715-585-151; RRID: AB_2340855
Alexa 488 donkey anti goat	Jackson Immuno Research	Cat#: 705-545-147; RRID: AB_2336933
Alexa 647 donkey anti rat	Jackson Immuno Research	Cat#: 712-605-153; RRID: AB_2340694
Alexa 647 donkey anti goat	Jackson Immuno Research	Cat#: 705-605-003; RRID: AB_2340436

(*Continued on next page*)

Continued

REAGENT or RESOURCE	SOURCE	IDENTIFIER
Alexa Fluor 488 conj. Streptavidin	Jackson Immuno Research	Cat#: 016-540-084; RRID: AB_2337249
Bacterial and virus strains		
pCL-vector encoding PDGFB, cre-NLS, copGFP and puromycin-resistance	Sirion Biotech	N/A
Chemicals, peptides, and recombinant proteins		
Tamoxifen	Sigma	Cat#: T5648
Lipopolysaccharides	Sigma	Cat#: L4391
5-Chloro-2′-desoxy-uridine, (CldU)	Sigma	Cat#: C6891
5-Iodo-2′-desoxy-uridine, (IdU)	Sigma	Cat#: I7125
Tissue-Tec O.C.T	Sakura-Finetek	Cat#: 4583
Fluorescence Mounting Medium	Dako	Cat#: S3023
SYTOX Blue dead cell stain	ThermoFisher Scientific	Cat#: S34857
Phusion HF Buffer Pack	New England Biolabs	Cat#: B0518S
DMEM	Milipore	Cat#: FG0415
Dulbeccos MEM (10x)	Biochrom	Cat#: F0455
FBS superior	Biochrom	Cat#: F0615
DMEM F12	ThermoFisher Scientific	Cat#: 11320-074
B27-	ThermoFisher Scientific	Cat#: 17504044
EGF	PeproTech	Cat#: 100-15
FGF	PeproTech	Cat#: 100-18B
Critical commercial assays		
MaxFluo Mouse-on-Mouse Fluorescence Detection Kit	Dianova	Cat#: MF01
Deposited data		
scRNA-seq Raw and analyzed data	This paper; https://www.ebi.ac.uk/ena	Accession#: PRJEB24104
Single-cell RNA-seq of mouse cerebral cortex	Zeisel et al, 2015	Accession#: GSE60361
Mapping microglia diversity in the human brain through the integration of high-dimensional techniques	Sankowski et al., 2019	Accession#: GSE135437
Single-cell RNA-seq from high grade primary glioma samples	Wang et al., 2019	Accession#: EGAS00001003845
Copy number variation Raw data	http://www.ebi.ac.uk/arrayexpress/	Accession#: E-MTAB-7649
Experimental models: cell lines		
GL261	National Cancer Institute, NCI-Frederick	RRID:CVCL_Y003
p53KOPDGFB primary mouse GBM cells	Established at LMU Clinics Munich,	Mastrella et al., 2019
cdkn2aKOEGFRvIII primary mouse GBM cells	Established at LMU Clinics Munich,	Mastrella et al., 2019
NCH644 primary human GBM cells	Campos et al., 2010; https://doi.org/10.1158/1078-0432.CCR-09-1800	RRID: CVCL_X914 and Mastrella et al., 2019;
Line#2 primary human GBM cells	Binda et al., 2017; https://doi.org/10.1158/0008-5472.CAN-16-1693	Mastrella et al., 2019
GBM14 primary human GBM cells	Drachsler et al., 2016; https://doi.org/10.1038/cddis.2016.102	Mastrella et al., 2019 https://doi.org/10.1158/0008-5472.CAN-18-0881
Experimental models: organisms/strains		
Nes-cre/ERT2/7Vtlr	This paper, Giachino and Taylor, 2009; https://doi10.1111/j.1460-9568.2009.06798.x	N/A
Nes-cre/ERT2KEisc/J	The Jackson Laboratory	RRID:IMSR_JAX: 016261
Sox2-cre/ERT2Hoch/J	The Jackson Laboratory	RRID:IMSR_JAX: 017593

(*Continued on next page*)

Continued

REAGENT or RESOURCE	SOURCE	IDENTIFIER
Sox2-IRES-cre/ERT2	Riccardi et al., 2016; https://doi.org/10.1186/s12864-016-2620-7	N/A
Cx3cr1-cre/ERT2Litt/ WganJ	The Jackson Laboratory	RRID:IMSR_JAX: 021160
Pdgfrb-cre/ERT2 Csln/J	The Jackson Laboratory	RRID:IMSR_JAX: 030201
Cdh5-cre/ERT2Rha	Sörensen et al., 2009; https://doi: 10.1182/blood-2008-08-174508.	N/A
Flt3-cre/Ccb	Benz et al., 2008, https://DOI:10.1084/jem.20072168	N/A
Gt(ROSA)26Sor-CAG-tdTomato/Hze	The Jackson Laboratory	RRID:IMSR_JAX: 007909
Gt(ROSA)26Sor-DTA/Mrc/J	The Jackson Laboratory	RRID:IMSR_JAX: 010527
Gt(ROSA)26Sor-ACTB-2tdTomato-EGFP/Luo/J	The Jackson Laboratory	RRID:IMSR_JAX: 007676
Sox2-loxP/Lan/J	The Jackson Laboratory	RRID:IMSR_JAX: 013093
Cx3cr1-GFP/Litt/J	The Jackson Laboratory	RRID:IMSR_JAX: 005582
Ccr2-eGFP/Cln/J	The Jackson Laboratory	RRID:IMSR_JAX: 027619
Spi1-GFP/Nutt	Nutt et al., 2005; https://DOI:10.1084/jem.20041535	N/A
Cdkn2a/Rdp/Nci	Serrano et al., 1996; https://doi.org/10.1016/S0092-8674(00)81079-X	N/A
Recombinant DNA		
pBABE-zeo	Addgene	RRID:Addgene_1766
pCMV-VSV-G	Addgene	RRID:Addgene_8454
Software and algorithms		
Graph Pad Prism v.7	http://www.graphpad.com	RRID:SCR_002798
ImageJ	http://www.imagej.net	RRID:SCR_003070
IMARIS Digital Imaging software	http://www.bitplane.com/imaris/imaris	RRID:SCR_007370
Leica Application Suite X	https://www.leica-microsystems.com/products/microscope-software/details/product/leica-las-x-ls/	RRID:SCR_013673
FlowJo	https://www.flowjo.com/solutions/flowjo	RRID:SCR_008520
FCS Express	https://denovosoftware.com/?gclid=EAIaIQobChMI36rn3-Dd3AIV2ud3Ch27lw2oEAAYASAAEgLbRvD_BwE	RRID:SCR_016431
zUMIs pipeline	Parekh et al. 2018 DOI: 10.1093/gigascience/giy059	https://github.com/sdparekh/zumis
Bioconductor	https://bioconductor.org	RRID:SCR_006442
Scran	Lun et al., 2016	N/A
limma trend	Law et al., 2014	N/A
rescaleBatches	Haghverdi et al., 2018	N/A
ReactomePA	Yu and He, 2016	N/A
Stereo Investigator	http://www.mbfbioscience.com/stereo-investigator	RRID:SCR_002526

RESOURCE AVAILABILITY

Lead contact

Further information and requests for resources and reagents should be directed to and will be fulfilled by the Lead Contact, Rainer Glass (rainer.glass@med.uni-muenchen.de).

Materials availability

This study did not generate new materials. Availability of transgenic mouse models is regulated by material transfer agreements with the scientists creating the models.

Data and code availability

- Copy number variation and scRNA-Seq source data have been deposited at ArrayExpress and at European Nucleotide Archive (ENA) and are publicly available under the accession numbers ArrayExpress: E-MTAB-7649 respectively ENA: PRJEB24104. This paper also analyzes existing, publicly available data. These datasets' accession numbers are provided in the Key resources table.
- This paper does not report original code.
- Additional scripts used to generate figures reported in this paper are available at (https://github.com/sdparekh/zumis) and (https://bioconductor.org/packages/release/bioc/html) and their use is described in the STAR methods.
- Any additional information required to reproduce this work is available from the Lead Contact.

EXPERIMENTAL MODEL AND SUBJECT DETAILS

Mice

Animal experiments were carried out in compliance with the German law on animal welfare, and animal protocols were approved by local authorities "Regierung von Oberbayern" in Munich or the "Ministerium für Energiewende, Landwirtschaft, Umwelt, Natur und Digitalisierung des Landes Schleswig-Holstein (MELUND)" Kiel, Germany as required. Mice were housed in standardized cages in the animal centers of the Ludwig-Maximilians-University (LMU) Munich, the University of Kiel or the animal experiment center of the Renmin hospital of Wuhan University, received chow ad libitum and were kept under a circadian rhythm with 12 h light and dark cycles. Mice used for experiments were of both sex and older than postnatal day 100. Tumor-take in all neuro-oncological models was $\geq$ 98%; mice were only excluded from analysis when no tumor-growth observed. A comprehensive list of all transgenic mouse strains used for this study is given in the Key resources table and more explanations can be found in Table S1 (including identifiers, references and basic scientific background) and in previous studies (Benz et al., 2008; Nutt et al., 2005; Serrano et al., 1996; Sörensen et al., 2009). Additional information is provided in Table S2, which provides (sequentially throughout all relevant figures) information on cross-breeding of strains, specific scientific background and summarizes the particular experimental use of each model.

Human glioblastoma specimens

Glioblastoma samples were obtained from the University Hospital, LMU Munich (under the project number 599-16, 18-304) in agreement with all ethical standards; informed consent according to the guidelines of the local Insitutional Review Board was obtained and the ethical standards of the Helsinki Declaration were fulfilled. A comprehensive list of all human material analyzed in this study is provided in Table S3 (including age and sex).

Cell culture

Mouse or human GBM cells (GL261; $p53^{KO}$, PDGFB; $cdkn2a^{KO}$, EGFRvIII, GBM14, NCH644 or Line#2) were maintained in DMEM containing 1× MEM non-essential amino acids, 5% penicillin-streptomycin, and 10% fetal bovine serum. Cell-line authentication confirmed the identity of GL261 cells. All other mouse transgenic or human primary GBM cell cultures were previously described (Binda et al., 2017; Campos et al., 2010; Drachsler et al., 2016; Mastrella et al., 2019) as listed in the Key resources table and were confirmed to be mycoplasma-free. Cells were propagated under neurosphere cell culture conditions in DMEM/F12 (Invitrogen) containing supplement (B27), growth factors (20 ng / ml EGF and FGF) and additives (0.2 mM glutamine, 5% penicillin-streptomycin). Copy number analysis of all primary glioblastoma cells was performed using Affymetrix Cytoscan HD Microarray.

METHOD DETAILS

Tumor inoculation and tamoxifen treatment

Surgical procedures were performed as described previously (Stock et al., 2012): Anesthetized transgenic or wild-type mice were immobilized and mounted into a stereotactic head holder (David Kopf Instruments), in the flat-skull position. Approximately 1.5 mm lateral to the bregma a 1-μL 30 G gas-tight syringe (Hamilton) was then inserted to a depth of 4 mm, retracted to a depth of 3mm from the dural surface and cell suspensions were injected. Mice received murine GBM cells (GL261, $1x10^5$ cells / 1 μl), which reliably generate angiogenic tumors that have a consistent histopathological pattern and growth-rate in cohorts of mice (Stock et al., 2012). All orthotopic tumor models were obtained with animals older than postnatal day 100 (P100), which thereby excludes any pathologically relevant contribution of NPC (Stock et al., 2012).

We administered 75 mg Tamoxifen TAM/kg body weight (dissolved in corn oil) in a single intraperitoneal. injection per day and performed three consecutive injections per animal (see below). Controls included injection of corn oil (without TAM). In other negative controls, we administered TAM to transgenic mice deficient for the creER2 allele. Animals of both sexes were used for this study and mice were randomly allocated to the respective experimental groups.

Generation of mouse bone marrow chimeras

Bone marrow (BM) chimeras were generated as described (Grathwohl et al., 2009). Donor cells were obtained from tibia and femur. Briefly, after lethal irradiation (950 rad) mice were intravenously injected with BM from donors and treated with antibiotics (enrofloxacin 0,01 mg/ml in drinking water; Baytril 25, Bayer for 4 weeks). Successful BM reconstitution was defined as >94% engraftment of blood leukocytes by FACS analysis. Furthermore, efficient engraftment of BM and abundant accumulation in experimental GBM (Glass and Synowitz, 2014) was ready.

In-vivo multiphoton laser scanning microscopy

Experiments were carried out in male nes::creER2, R26-RFP mice. Cranial window preparation and stereotactic cortical tumor implantation was performed as previously described (von Baumgarten et al., 2011). Briefly, mice were deeply anesthetized with intraperitoneal injection of MMF (Midazolam 5 mg/kg body weight, Medetomidin 0.05 mg/kg, and Fentanyl 0.5 mg/kg body weight). Skull and dura mater were removed by microsurgery then the brain was covered using a 6 mm diameter transparent window (ThermoFisher Scientific). Two weeks later, the cover glass was carefully removed and 50.000/μl GL261 cells were stereotactically injected in an intraparenchymal depth of 1 mm. After tumor implantation, a new, sterile cranial window was attached.

We used a multiphoton LaVision Biotech TrimScope I system connected to an upright Olympus microscope, equipped with a Mai-Tai Laser (690-1040nm; Spectra Physics) and a 20× water immersion objective (numerical aperture 0.95, Olympus). Single images were acquired from 300 μm depth, with z-interval of 2 μm. The excitation wavelength was 920 nm, with 1024 ×1024 pixels and signal detected by PMTs (G6780-20, Hamamatsu). Imspectro (LaVision Biotech) was used as acquisition software. For cerebral vessel visualization, we injected 0.1 ml 10 mg/ml FITC-dextran (2M molecular weight, green) through the mouse tail vein. Identical anatomical regions were followed over time and identified by the vessel structure. Mouse body temperature was kept constant using a heating pad with temperature tester. Mice were anesthetized by isoflurane under a constant flow from 0.8% to 2.0% (as low as possible according to the physical condition of the mouse). The laser power was adjusted to avoid photo-toxicity. After original images were acquired using Imspector Pro, Bitplane Imaris Software was used for further analysis. To obtain high-quality images, brightness, contrast, or color balance were regulated manually for the whole images. Maximum Intensity Projection (MIP) function was used to obtain 2-dimensional images.

Temporary middle cerebral artery occlusion (tMCAo) as ischemic injury

Mice were anesthetized and focal cerebral ischemia was induced by introducing a silicone-coated 8-0 Doccol monofilament (Sharon) via the internal carotid artery. For sham operations, the filament was shorty inserted into the internal carotid artery, advanced, and the retracted immediately. Mice were kept warm during the procedure. The incision was closed temporarily, and reopened for removal of the filament after one hour. After withdrawal of the filament, the internal carotid artery was occluded with a permanent suture and the incision was closed. Mice were tested for neurological deficits directly after the procedure, and every 24 hours until 7 days after induction of ischemia. Animals were rated from having no observable deficit, to moderate or severe deficits. Failure to extend to forepaw when suspended vertically was graded as mild injury, circling to the contralateral side was graded as moderate injury, and loss of circling or righting reflex was graded as severe.

LPS treatment

To investigate the neuroinflammatory response, Lipopolysaccharides (LPS;) was injected intracerebrally at 1 mg/ml. Mice were anaesthetized, immobilized and mounted into a stereotactic head holder (David Kopf Instruments), in the flat-skull position. Approximately 2.0 mm lateral, 1.5 mm anterior to the bregma a 1-μL 30 G gas-tight syringe (Hamilton) was then inserted to a depth of 4 mm, retracted to a depth of 3 mm from the dural surface and 1 μl LPS solution was injected. On day 0, 1 and 2, 75 μg TAM/g body weight was administered i.p. and the animals were collected on day 7 for immunohistological analysis.

Genetically induced GBM

A retroviral vector for the expression of a mature PDGFB isoform was expressed under a human GFAP promoter construct within in a retroviral vector backbone; viruses were pseudotyped with a VSV-G envelope, concentrated (5×10^8 cfu/ml) and delivered (with the following stereotactic coordinates relative to the bregma: anterior, 0.6 mm; mediolateral, 1.6 mm; dorsoventral, 2 mm) into the SVZ of young (P30) cdkn2a-deficient mice. Development of a tumor mass was observed within 40 to 60 days after the operation.

Administration of thymidine analogs

Equimolar solutions of two different thymidine analogs (23 mg /ml 5-Chloro-2′-desoxy-uridine, CldU, and 17 mg / ml 5-Iodo-2′-desoxy-uridine, IdU; both from Sigma) were generated (Llorens-Martín and Trejo, 2011). Animals we intraperitoneally injected with 2.5 ml / kg CldU or 2.5 ml / kg IdU.

Histology and immunohistochemistry

In vivo experiments with GBM models were stopped 7 days, 14 days, or 21 days after tumor induction (indicated as days post-operative, DPO, throughout this study). Therefore, mice were anesthetized at 7DPO, 14DPO or 21DPO and perfused with PBS followed by 4% PFA (in PBS). Brains were dissected and kept in a 4% PFA solution for 2 days at 4°C, then specimens were dehydrated in a 30% sucrose solution (in PBS), frozen in cryo-embedding solution (Tissue-Tec O.C.T.Sakura-Finetek) and stored at −20°C. Frozen brain

blocks were cut into 40-μm horizontal sections and preserved as free-floating sections in a 24-well-plate filled with cryoprotectant (ethylenglycol, glycerol and 0.1 M phosphate-buffer in a 1:1:2 solution at pH 7.4).

Floating sections stored in cryopreservative solution were extensively washed (1x PBS); for CldU or IdU visualization pretreatment of the tissue with 1 N hydrochloric acid for 30 minutes at 37°C, followed by rinsing in borate buffer for an additional 10 minutes was performed; all sections were immersed for 1 hour at room temperature in blocking-solution: 1x PBS containing 5% normal donkey serum (Jackson Immuno-Research) and 0.3% Triton-X (Fluka) and incubated overnight at 4°C with primary antibodies (see Key resources table).

After extensive washing, sections were incubated for 3 hours at room temperature with species-specific secondary antibodies (see Key resources table). All antibodies were diluted in blocking solution. After staining, tissue was mounted in Fluorescence Mounting Medium (Dako). For CD68- and IdU-staining the MaxFluo Mouse-on-Mouse Fluorescence Detection Kit (Dianova) was used (Goodpaster and Randolph-Habecker, 2014).

Microscopy, image-processing and quantification

A Zeiss Axioskop 2 or Axiovert 135 was used for light microscopy or fluorescence microscopy. Confocal microscopy was performed using a TCS SP8 microscope (Leica). Confocal image stacks were processed with the ImageJ software, Leica Application Suite X (Leica), and the IMARIS Digital Imaging software (Bitplane). Cells were interpreted as perivascular if they were located in a distance of maximally 1 μm to a von Willebrand Factor (vWF)-positive vascular structure. Quantifications were conducted in the tumor area (visible as area with high nuclear density after nuclear staining with DAPI) in four randomly selected view-fields per tissue-section. As 4 sections were analyzed per animal, a total of 48 optical fields per animal were evaluated for every immunofluorescence labeling experiment.

Tumor size quantification

Tumor size determination was performed as described (Stock et al., 2012). Two weeks after orthotopic implantation of GFP or DsRed expressing tumor cells, brains were sectioned and every 6th axial section 1.8 to 4.2 mm from dural surface was sampled (representing the area that was infiltrated by the tumor). Tumor volume was quantified according to the Cavalieri principle by determining the tumor area in every sampled brain slice. Stereotactical coordinates of brain slices containing GBM were determined and used to calculate a Z-axis of the experimental brain tumor. This Z-axis was multiplied with the average brain tumor area per brain-section to obtain a tumor volume per animal.

Stereological analysis of vasculature

Vessel-length, -length-density and number of branch points were investigated in the tumor area after vWF-immunofluorescence staining on every 12th section. Vessel-length-density was determined using the space ball method of the StereoInvestigator Software 10.21.1 (MicroBrightField Bioscience) connected to an Olympus-BX53-microscope (Olympus Europe) and a motorized object table (MicroBrightField Bioscience).

Single cell preparation and staining for flow cytometry

Nestin-cre::ER2, R26-RFP mice were inoculated with GFP-expressing GBM cells and TAM injected (as described above). At 7DPO (n = 3) or 21DPO (n = 3) mice were killed, brains were harvested and the tumor mass was microdissected under a fluorescence-stereomicroscope (Leica). Single cells were obtained by triturating dissected GBM in PBS and subsequent treatment with 1mg/ml collagenase-I followed by several wash-steps and filtering through a 40μm cell strainer.

Fluorescence activated cell sorting

FACS sorting was done using a FACSAria III (Becton Dickinson,) equipped with 4 Lasers (50mW 405nm, 20mW 488nm, 50mW 561nm and 18mW 633nm) and operated with a 70μm Nozzle at 88kHz on single cell sort mode. Cells were pregated using FSC/SSC debris exclusion, FSC-W singlet discrimination and sorted for living (excluding SYTOX Blue dead stained cells; ThermoFischer Scientific) RFP+ tumor-derived cells into a 96 well plate. Simultaneously, GFP+ glioma cells were detected (verifying intratumoral localization of RFP+ cells).

Single-cell RNA-Seq data generation

Single-cell data was generated using a slightly modified SCRB-seq protocol (Soumillon et al., 2014). Briefly, RFP+ cells were sorted as described above into 96-well plates (Eppendorf) containing 5 μl of a 1/500 dilution of Phusion HF buffer (NEB). RNA was reverse transcribed using barcoded oligo-dT primers carrying cell-specific barcodes and unique molecular identifiers (UMIs). Next, cDNA was pooled and unincorporated primers digested using Exonuclease I (ThermoFisher Scientific). After pooled cDNA was amplified using KAPA HiFi (KAPA Biosystems), libraries were generated using the Nextera XT Kit (Illumina). Libraries were sequenced on a HiSeq1500 (Illumina) for 16 cycles in read 1 to decode barcodes and UMIs and 50 cycles in read 2 to obtain the cDNA fragment.

Single-cell RNA-Seq data processing

Raw sequencing data was processed using the zUMIs pipeline with default filtering settings (available under: https://github.com/sdparekh/zUMIs). Reads were mapped against the Mouse genome (mm10) and tdTomato with RefSeq gene models (Version 85).

We filtered out cells that were more than 3 absolute deviations away from the median of UMI or gene count per batch, allowing us to keep 170 out of 180 cells with on average 26,000 UMIs/ cell. For comparison, we downloaded the raw data from (Zeisel et al., 2015) and processed them with zUMIs, keeping cells with 3,000-50,000 UMIs. Normalization was performed with scran with clustering (Lun et al., 2016). We used normalized, log transformed counts as our measure for expression levels for all transcriptome analyses. Next, we used the function rescaleBatches from the Bioconductor package batchelor (Haghverdi et al., 2018) to remove the plate-effect. The combined data sets were visualized using t-SNE dimension reduction (Krithje, 2015) with a perplexity of 30 on the first 10 principle components based on the 1,000 most variable genes.

To determine to which of the known brain cell types our RFP+ avascular cells show the highest similarity, we used an implementation of Breiman's random forest algorithm (Breiman, 2001). We trained a supervised predictive model with 200 decision trees for the seven main subgroups specified in (Zeisel et al., 2015) on genes that were also detected in the RFP+ cells. We applied this classifier to obtain prediction proportions for each single cell. Furthermore, we used the data from sorted murine cortical cells (Zhang et al., 2014) expressed marker genes for the relevant cell types.

Next, we conducted differential gene expression analysis, comparing RFP+ avascular cells between time points also adding the batch to the model using limma-trend (Law et al., 2014). We used the bioconductor package ReactomePA for gene set enrichment analysis (Yu and He, 2016).

Human single cell data processing

We received raw cellRanger count matrices for the 10X single cell RNA-seq data for patient samples SF11136, SF11644, SF11949, SF11956, SF11964, SF11977 and SF11979 (Wang et al., 2019). In order to remove noise from ambient RNA and barcode swapping, we used the background correction from CellBender. The resulting corrected count matrices were then filtered to keep only cells with at least 1000 detected genes and a gene is called detected if it had at least one count. The log-normalized data were then subjected to cell type classification with singleR (Aran et al., 2019) using the data from (Zhang et al., 2014) as reference. The cell type classes that we can distinguish with this reference are astrocytes, neurons, endothelial cells, oligodendrocytes and microglia/macrophages. Because TAMEPs are more myeloid-like, we used this classification to remove all unwanted cell types to only keep myeloid-like cells. The Sankowski et al. data (Sankowski et al., 2019) were downloaded from the Gene Expression Omnibus (accession number: GSE135437) and processed in the same way except for the background correction.

Data from patient SF11644 were analysed in more detail: cell clusters were identified using Seurat3 (Stuart et al., 2019), based on 30 PCs of the 2000 most variable genes and a resolution of 0.1. Furthermore, we used one-class logistic regression (Malta et al., 2018) to quantify the similarity of the human patient-derived cells to mouse TAMEPs. First, we identified orthologous genes between human and mouse with ensembl biomart. Next, we only used mouse genes from our TAMEP scRNA-seq data that have a human orthologue and are expressed in at least 5% of the myeloid cells in patient SF11644 to derive a one-class predictor. We then used this predictor to obtain a TAMEP index for the myeloid cells from patient SF11644.

QUANTIFICATION AND STATISTICAL ANALYSIS

No statistical methods were used to predetermine sample sizes, but our sample sizes are similar to those previously reported (Stock et al., 2012); experimental groups were not blinded. In all Figures, the data presented are representative of at least 3 independent experiments. Data were analyzed with the GraphPad Prism software (version 5.04; GraphPad Software Inc., La Jolla, California, USA). Experimental groups comparing two samples were evaluated with an unpaired, non-parametric student's t-test, while experimental groups containing multiple samples (>two groups) were tested for statistical significance by one-way ANOVA together with a Newman-Keuls post-hoc test. Bar-diagrams include data-points for individual experiments or individual mice (as specified) and present mean-values ± standard-deviation of the mean; statistical significance was assumed if $P < 0.05$; P-values were shown in figures as *: $p<0.05$, **: $p<0.01$ and ***: $p<0.005$, ****: $p<0.0001$, N.S.: not significant. The exact values of n and the statistical analysis used are specifically indicated in each figure legend.